National University of Science and Technology
POLITEHNICA Bucharest
Doctoral School of Energy Engineering

DOCTORAL THESIS

ABSTRACT

INVESTIGATION OF MITIGATION METHOD FOR HYDRAULIC TURBINE DRAFT TUBE FLOW

INVESTIGAȚII ASUPRA METODELOR DE ÎMBUNĂTĂȚIRE A CURGERII ÎN ASPIRATORUL TURBINELOR HIDRAULICE

Author: Ing. Robert MITRUȚ

Scientifc Supervisor: Prof. dr. ing. Diana Maria BUCUR

BUCHAREST
2023

CONTENT

THESIS OUTLINE

The rotating vortex rope is associated with the vortex breakdown phenomenon which in theory is the effect of a stability loss of the flow. The loss of stability arise from an infinitesimal external disturbance which enter the fluid domain and develop in time and space. In the particular case of the hydraulic turbine flow, finding a solution to mitigate the development of the disturbances would eventually lead to new mitigation techniques to quench the rotating vortex rope. Thus, all its hazardous effects on the functionality of the turbines will be eliminated. The hydraulic turbines will therefore be capable to work in an extended domain of the Best Efficiency Point (BEP) delivering the power supply necessary to balance the electrical grid without the fatigue and cavitation induced by the rotating vortex rope. The mitigation techniques rely on the use of the linear global stability analysis to understand the mechanism which trigger the development of the external infinitesimal disturbances omnipresent in flow and its surroundings. The linear global stability analysis provides relevant insights that allow the identifying of areas that are particularly responsive to external influences, such as a water jet or stabilizer fins. These insights can inform strategic interventions aimed at mitigating RVR and enhancing flow stability.

Considering the aim of the present thesis, the content of the thesis is structured as it follows:

- Chapter I. Motivated by the vortex flow dynamics within hydraulic turbines, this chapter begins with a brief historical overview, tracing the earliest observations of the vortical structures and emphasizing their significance in the fluid dynamics field. Further, the actual context of the energy market highlighting the implications of intermittent injections of electricity into the power grid, produced by renewable energy sources, is discussed. The discussion subsequently shifts to the present role of hydroelectric power plans addressing the consequences of operating the hydraulic turbines in off-design conditions. A literature overview of the research carried out in the field of numerical simulations and experimental investigations to understand the flow dynamics in the hydraulic turbines draft tube is presented. It is shown that the underlying phenomena that leads to the apparition of the unstable vortical structures inside the hydraulic turbines may be studied using simplified flow configurations presenting the same structure at the basis. The chapter ends with an outline of the work done and the intermediate steps to reach the final objective.
- Chapter II. This chapter is dedicated to the mathematical formulation of the linear global stability framework, and it aims to lay the theoretical foundation used for the numerical simulations.
- Chapter III: Once the theoretical framework is explained, the natural question is how to put in practice these notions, so this chapter aims to explain the integration of the theory into practice. The numerical solvers which are used in the current thesis are described along with the turbulence models used (if it is the case) and the details of the numerical set-up.
- Chapter IV. It presents the numerical results of the flow inside a Francis hydraulic turbine model. The numerical simulations are carried out for steady-state and

unsteady-state turbulent flow configurations at three operating regimes, Best Efficiency Point, High Load and Part Load. The spatial structures of the vortical structures are shown here and the numerically obtained quantities such as the axial and radial velocity are validated against experimental data available in the literature. Additionally, the numerical frequency of the vortex rope is validated with the experimental frequency obtained using the experimental data.

- Chapter V. The complex flow configuration inside a hydraulic turbine is numerically analyzed from the perspective of a simplified flow configuration which lays on the same dynamics at the basis. The numerical simulations are carried out in a two-dimensional framework to study the dynamics of an incompressible laminar flow around a circular bluff-body. The numerical simulations are carried out for both steady-state and unsteady-state flow configurations and validated with available data in the literature for different values of the Reynolds number.
- Chapter VI. The results obtained in Chapter V are used to perform linear global stability analyzes. The outcomes deliver relevant information about the most receptive zones where an external force has the most impact in influencing the flow dynamics. Different control bluff-bodies of various shapes and dimensions are placed in these zones to mitigate the instabilities. The efficiency of such passive control techniques to mitigate the instabilities is analyzed at the end of the chapter.
- Chapter VII. The last chapter of the current thesis comprises the conclusions and observations of the thesis research work, highlights the personal contributions of the author to these research field and ultimately offers new perspectives to continue the work on the current subject.

1. INTRODUCTION

The hydraulic turbines are individually designed and constructed to meet the specific requirements and conditions of each power plant site. Implicitly, they are designated to work in optimum conditions, namely at the Best Efficient Point, delivering the maximum power output with maximum efficiency. Theoretically, in these conditions, the flow that exists the runner has only an axial component while the rotational component, i.e. the tangential velocity is zero. In reality, a residual swirl is observed at the runner outlet which prevents the separation of the flow from the draft tube surface and minimizes the hydraulic losses. While a small shift of the discharge around the nominal point is accepted to balance the power grid, further extensions are not recommended due to the risk of developing unwanted phenomena inside the draft tube such as the cavitation vortex

At the High Load (HL) operating condition, i.e., the discharge is higher than the nominal one ($Q > Q_{BEP}$), the tangential component of the absolute velocity, c_θ, and the runner velocity, $\mathbf{u}$ are in opposite directions. In this case, a pulsating vortex rope develops rotating in the opposite direction of the runner. Compared to the RVR, the pulsating vortex rope presents a nearly axis-symmetric shape. In both cases the vortex rope induces large pressure fluctuations, vertical movements of the runner, vibrations and pounding noises which lead to the efficiency

loss and cavitation. An extreme phenomenon of resonance may occur if the pressure fluctuations vibrations align with the natural frequency of the whole installation [12].
Consequently, the dynamics of the flow inside the draft tube of hydraulic turbines is the subject of numerous experimental and numerical studies. Due to the costs associated to the investigations, limited and difficult access to the hydraulic turbine components and flow complexity, the RVR is studied in several research in simplified geometries in order to understand its physics. The apparition of the RVR is attributed to the Vortex Breakdown (VB) phenomenon which occurs in a wide range of applications. The VB phenomenon was first studied by Peckham and Atkinson in an aerodynamic study regarding the flow over a delta wing [21]. Transition to turbulence

The flow through the turbines can be attributed to the open flow class, where the fluid particles are in a state of constant entry and exit of the experimental domain [18]. Such flows, as M. Kurosaka et. al and O. Reynolds remarked, are constantly submitted to infinitesimal external perturbations which in certain conditions can develop an amplification mechanism to destabilize the flow [24], [29].

The global linear stability approach is suitable for strongly nonparallel flows, with the key assumption that the basic state is a truly parallel flow [31]. This assumption was extended to unsteady, i.e. time dependent, laminar flow by using the mean, i.e. time averaged, flow. This approach was successfully applied in applications as two-dimensional vortex shedding behind a circular bluff bodies or three-dimensional spiral vortex breakdown flows [32], [33]. The results reported in [32], [33] confirmed that linear global stability analysis around the mean correctly predicts the frequency of the instabilities. However, it seems that the base flow computed far away from the insertion points of the external disturbances yield natural frequencies and the linear global stability analysis fails to predict instability frequency. Despite this inconvenience, the eigenvalues computed by the linear global stability analysis around the base flow provide with good accuracy the growth rate of the instability which determines whatever the flow is stable or unstable.

Understanding the underlying phenomenon which lead to the apparition of the vortex rope would eventually result in active and passive techniques such as water jets to control and optimize the flow in order to mitigate the pressure fluctuations and increase the operating range of the hydraulic turbines in optimal conditions [40]. Implementing such measures would ultimately lead to a prolonged lifespan of the hydraulic turbine, improved efficiency, and cost savings by minimizing downtime and maintenance expenses.

1.1. THESIS OBJECTIVE

In this context, the present thesis aims to investigate the underlying phenomena that give rise to the formation of the vortex rope and to develop mitigation techniques for the draft tube flow. In the first stage, the numerical simulations of a flow inside a model of Francis turbine are performed using the free open-source Computational Fluid Dynamics (CFD) software Code_Saturne. Due to the high computational requirements in terms of resources and time, the flow inside the turbine is numerically simulated using only specific parts of the hydraulic turbine. Numerical simulations are consequently performed in a reduced geometry consisting of a runner passage and the draft tube cone and using the full draft tube geometry. The flow is

investigated for three representative operating regimes, namely Best Efficiency Point (BEP), High Load (HL) and Part Load (PL) and validated against experimental data. The intricacy of the geometry associated with the complexity of the flow suggests that is more convenient to study mitigation techniques of the RVR using simplified flow configurations. Such an example is the flow around a bluff-body which, same as the flow in hydraulic turbine, belongs to the open flows category and presents similar flow development. Therefore, the second stage of the numerical analysis performed in the present thesis aims to study the dynamics of a two-dimensional laminar flow obscured by a circular bluff-body at different values of the Reynolds number.

2. THEORETICAL BACKGROUND

2.1. GOVERNING EQUATIONS

In a general concept, the laminar motion of fluids is described by the non-linear system of partial differential equations (PDEs), namely the Navier-Stokes equations

$$\frac{\partial \mathbf{u}}{\partial t} + \mathbf{u} \cdot \nabla \mathbf{u} = -\nabla p + \frac{2}{\mathrm{Re}} \nabla \cdot D(\mathbf{u}) \tag{2.1}$$

$$\frac{\partial \rho}{\partial t} + \nabla \cdot (\rho \mathbf{u}) = 0 \,. \tag{2.2}$$

where $\mathbf{u}$ is the velocity field, p is the pressure, Re is the Reynolds number, ρ is the density and $D(\mathbf{u})$ is the rate-of-strain tensor.

2.2. LINEARIZATION STRATEGY

A linear stability analysis is conducted using the Linearized Navier-Stokes Equations (LNSE). To study the dynamics of the LNSE, it is considered that the flow is initially found in an equilibrium state which can be either steady, i.e. time-independent or unsteady (periodic), i.e., time-dependent. This equilibrium state is referred to as a "*base*" flow. Further, in the framework of the linear stability analysis, it is assumed that the flow can be decomposed into the *base* flow upon which three-dimensional disturbances are permitted to develop

$$\mathbf{u}(\mathbf{x},t) = \mathbf{u}_b(\mathbf{x}) + \varepsilon_d \mathbf{u}'(\mathbf{x},t); \quad p = p_b(\mathbf{x}) + \varepsilon_d p'(\mathbf{x},t) \tag{2.3}$$

where the subscript b denotes the base flow components while the quantities with apostrophe are the disturbance components designated to destabilize the flow. The ε_d term is the amplitude of the disturbance. Inserting equations (2.3) into equations (2.1) and (2.2) yields the governing equations for a disturbed flow.

The disturbance components are written as an amplitude with a spatial-temporal exponential variation

$$\boldsymbol{q}'[\mathbf{u}', p'](\mathbf{x}, t) = \tilde{\boldsymbol{q}}[\tilde{\mathbf{u}}, \tilde{p}]^T(\mathbf{x}) e^{i\Theta + \omega_e t} + c.c. \tag{2.4}$$

where the superscript ~ stands for the eigenmodes, Θ changes as a function of the considerations about the directional flow homogeneities, ω_e is a complex eigenvalue while *c.c.* is the complex conjugate. The eigenvector $\tilde{\boldsymbol{q}}$ corresponding to the leading eigenvalue ω_e is called a *global eigenmode* and its spatial structure reveals the way disturbances are driven. If equation (2.4) is introduced into the disturbed flow equations, it is easily observable that the eigenmodes and eigenvalues are basically the solution to the following eigenvalue problem (EVP)

$$\omega_e \tilde{\mathbf{u}} = LNS_{\mathbf{u}_b}(\tilde{\mathbf{u}}, \tilde{p}) \tag{2.5}$$

As mentioned above ω_e is, in general, a complex quantity of the form

$$\omega_e = \omega_r + i\omega_i \tag{2.6}$$

The real part of the eigenvalue is the temporal growth rate of the disturbance whereas the imaginary part represents the frequency. For a real part below zero, $\omega_r < 0$, the system is stable while for a positive real part, $\omega_r > 0$ an unstable and self-sustained oscillation of frequency ω_i is observed, leading to the instability of the flow. A third, special, case of neutral stability condition where the flow is marginally stable and the disturbance has a purely harmonic evolution in time, i.e. $\omega_r = 0$, may be found during the LSA [41]. In this situation the disturbance is neither dumped nor amplified. The procedure of Giannetti and Luchini [35] leads to the definition of the *structural sensitivity* tensor. Due to mathematical reasons, it is more convenient to simply represent the norm of the structural sensitivity tensor, S_w, of which the maximum values indicate the so-called *wavemaker*

$$S_w(\mathbf{x}) = \|\mathbf{S}(\mathbf{x})\| = \frac{\left\|\mathbf{u}^{\dagger}(\mathbf{x})\right\| \left\|\mathbf{u}'(\mathbf{x})\right\|}{\left\langle \mathbf{u}^{\dagger}, \mathbf{u}' \right\rangle}. \tag{2.7}$$

This procedure identifies the most receptive locations where an external force may be imposed in order to modify the flow dynamics. In the present thesis, these locations are used as reference zones to insert different control bluff-bodies to modify the flow dynamics aiming to mitigate the instabilities and stabilize the flow. From a practical point of view, the sensitivity analysis may be used to determine the most receptive zones where an external force such as a water jet or a physical object such as stabilizers fins could be promptly used in order to eliminate the RVR and stabilize the flow. The outcome of this action would result in a longer lifespan of the hydraulic turbine, increased efficiency and reduced costs due to inactivity or maintenance.

3. NUMERICAL METHODS

Once the theoretical background is established, the natural question which arises is how to tackle the mathematical problems. Chapter III aims to explain the numerical methods and methodology used to obtain the solution to the linear global stability analysis. The flow chart presented in Figure 3.1 intends to offer a concise and precise visual representation of the of the numerical approach.

Computational Fluid Dynamics (CFD) is an essential tool within the realm of fluid mechanics that employs numerical methods and computational techniques to solve fluid flow problems. Within the present PhD thesis, the attention is focused mainly to open-source CFD

libraries that will be systematically introduced while giving in parallel theoretical notions about the main steps involved in numerical simulations, namely:

- pre-processing: creating the numerical model and the computational domain;
- processing: performing the numerical calculation;
- post-processing: analyzing and interpreting the numerical results.

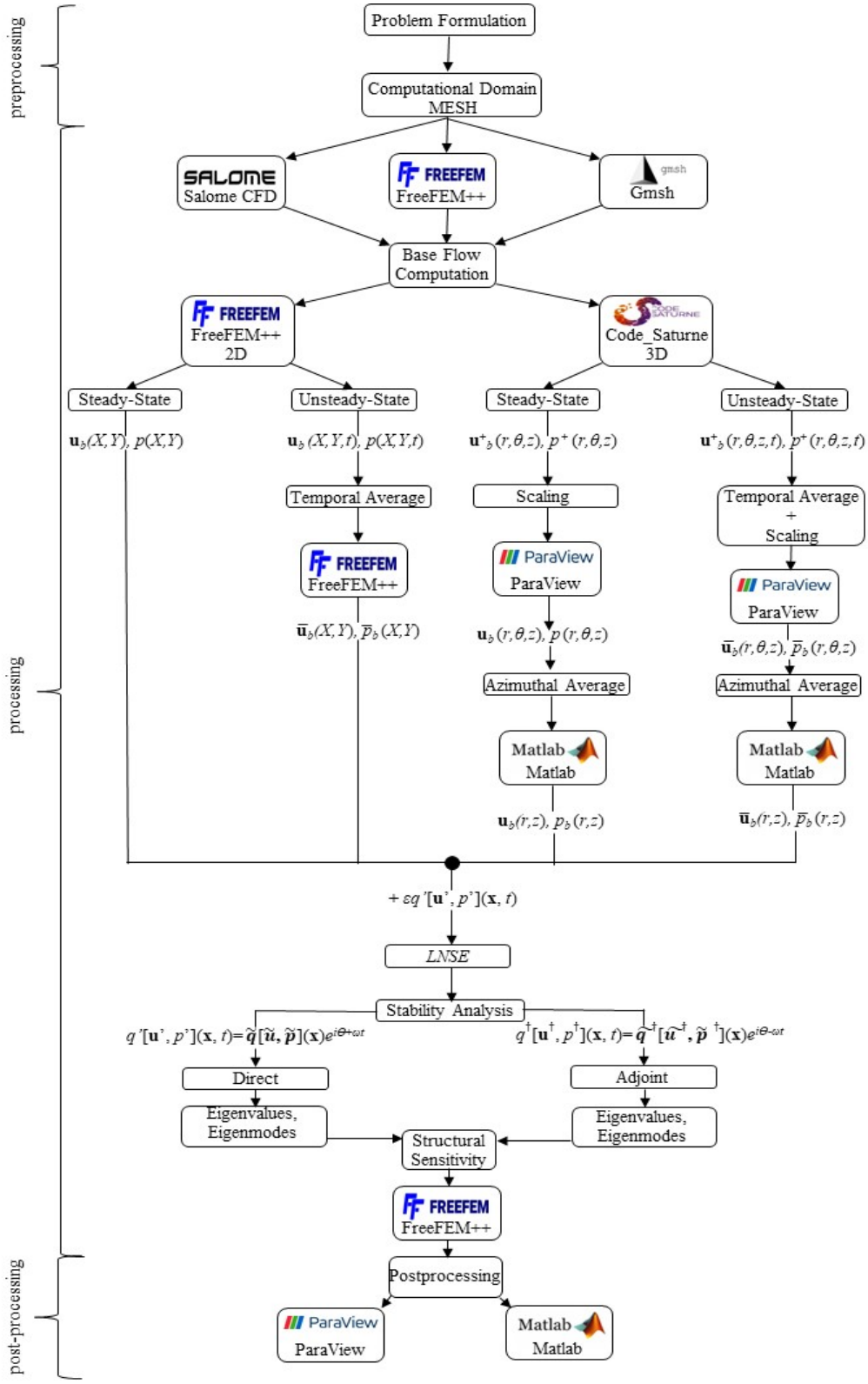

Figure 3.1. Schematic overview of the numerical approach.

3.1. PROCESSING

In order to study the stability properties of the flows involved in the current thesis, the solutions to the governing equations must be computed. A numerical approach of the partial derivatives equations (PDEs) implies the discretization in space and time of the quantities. The process involves partitioning the continuous spatial domain Ω into a discrete network of grid points and faces as explained earlier.

3.1.1. **Code_Saturne**

Code_Saturne is an open-source software developed by the Research and Development department of EDF (Electricité de France) since 1997, primarily designed for Computational Fluid Dynamics (CFD) applications. It is capable of addressing a wide area of fluid dynamics applications, ranging from 2D to 3D flows, including axisymmetric cases.

In turbomachinery simulations, Code_Saturne offers the flexibility to perform either approximated frozen rotor or full unsteady sliding mesh numerical simulations. This capability enables the seamless connection of different meshes and domains at domain interfaces [75]:

- *the frozen rotor* model offers computational efficiency and provides an approximate steady-state solution. However, it only partially considers the interaction between the two domains separated by the interface. Consequently, when employing this type of frame change, transient effects are not accounted for across the interface. This means that losses resulting from the mixing flow at the stationary-rotating boundary are not taken into account.
- the *sliding mesh* known also as the *transient rotor/stator*: In the input mesh(es), the interface between the rotor and stator domains must consist of boundary faces. Subsequently, during computation, these boundary faces at the interface are merged and converted into internal faces, a standard preprocessing step in typical calculations. The conventional approach to meet this requirement involves supplying separate meshes for each rotor or stator domain. However, it is permissible to include both sections within the same mesh, provided they remain topologically disconnected.

3.1.2. **FreeFEM++**

Recalling the information from Section 3.1, FreeFEM++ is an open-source partial derivative equations solver for linear and non-linear systems in 1D, 2D and 3D using the Finite Element Method and it has its own high level programming language based on C++ [49]. As it is based on a compilative-driven C++ language, in order to solve the problem it is necessary to import the appropriate libraries. A typical FreeFEM++ can be divided in the following steps:

1. define the numerical domain and generate the computational domain (mesh);
2. choose the Finite Element Space;
3. define the problem and boundary conditions using the weak formulation;
4. choose the solver and algorithms to discretizes the problem.

4. FRANCIS-99 TEST CASE

Chapter 4 is dedicated to the numerical simulations of the flow within the draft tube of a hydraulic turbine, with the aim of validating the numerical model against experimental data. The test case involves using a scaled-down model, at a 1:5.1 ratio to the actual prototype Francis turbine located at the Tokke Power Plant in Norway [81]. This model is situated at the Water Power Laboratory (WPL) within the Norwegian University of Science and Technology (NTNU). The model turbine consists of 14 stay vanes conjoined inside the spiral casing, 28 guide vanes, a runner with 15 splitters and 15 full-length blades, and an elbow-type draft tube.

4.1. EXPERIMENTAL SETUP

The experimental campaign involved the collection of most important operational parameters for the turbine, such as the flow rate, the turbine inlet pressure, the differential pressure between the spiral case inlet and draft tube outlet, atmospheric pressure, runner rotational speed, generator shaft torque, friction torque in the bearings, axial force on the turbine, and the opening angle of the guide vanes.

The pressure sensors employed in this study had distinct pressure ranges, with the draft tube sensors covering a range of 0-250 kPa, while the vaneless space sensors extended to a range of 0-1000 kPa. Two sensors, denoted as VL1 and VL2, were mounted in the area situated between the runner and the guide vanes (vaneless space). In contrast, the draft tube sensors were fixed to the draft tube wall. Within the draft tube, six pressure sensors (DT1, DT2, DT3, DT4, DT5, and DT6) were strategically positioned on the upper cone wall. These sensor placements were designed to capture both synchronous and asynchronous variations in the pulsations occurring within the draft tube. To achieve this, DT1 with DT3 and DT2 with DT4 were strategically placed 180° apart from each other. Additionally, DT5 and DT6 were positioned 180° apart from each other, aligned with DT2 and DT4. The pressure measurements within both the vaneless space and draft tube of the turbine were sampled at a high frequency of 5000 Hz.

4.2. SIMPLIFIED GEOMETRY OF THE RUNNER AND BOUNDARY CONDITIONS

As previously indicated, the simplified runner geometry comprises a runner passage, including a complete-length runner blade and a splitter runner blade, along with a section of the draft tube, as depicted in Figure 4.1.

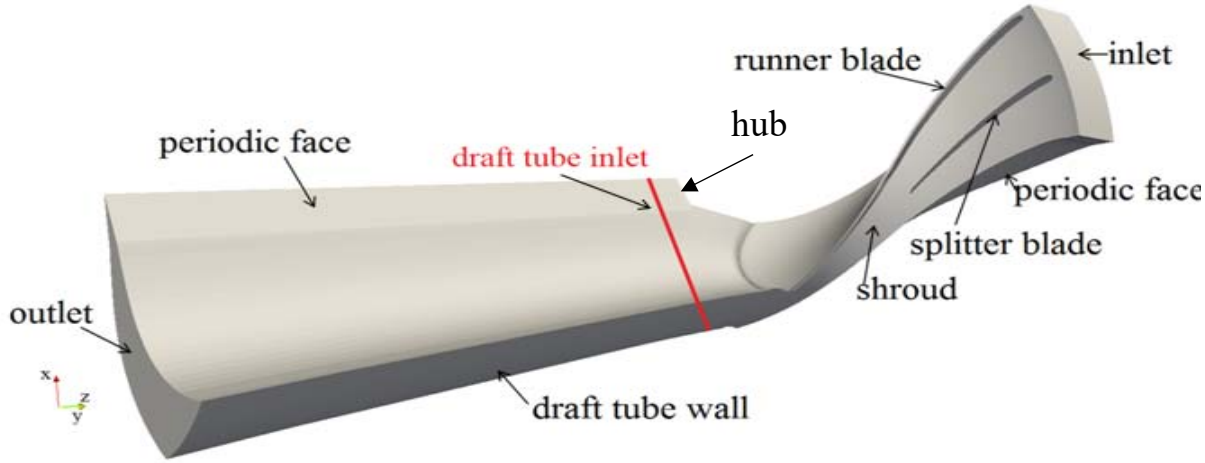

Figure 4.1. Simplified geometry of the runner and a part of the draft tube among the boundary surfaces [83].

The mesh of the simplified runner geometry is made of approximately 0.98 million of elements compared to the full runner versions which consists in about 4.05 million elements. An aspect also remarked in [75] is the presence of duplicate nodes which must be removed. Rather than being disregarded, these duplicate elements are interpreted as fixed walls by the Code_Saturne software

4.3. .FULL DRAFT TUBE GEOMETRY AND BOUNDARY CONDITIONS

The entire geometry of the draft tube accompanied by its boundary faces is presented in Figure 4.2.

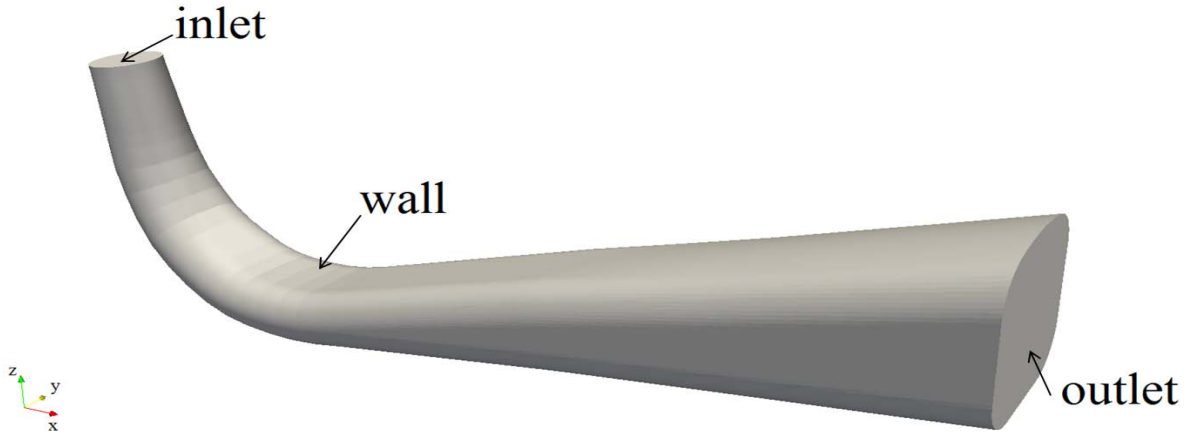

Figure 4.2. Computational domain of the full draft tube [83].

The velocity magnitude and axial velocity computed with the Frozen Rotor Turbomachinery model is shown in Figure 4.3. As it was expected, the steady-state, i.e. time-independent flow algorithm, is unable to capture the unsteady character of the flow inside the draft tube.

4.4. RESULTS FOR THE SIMPLIFIED GEOMETRY OF THE RUNNER

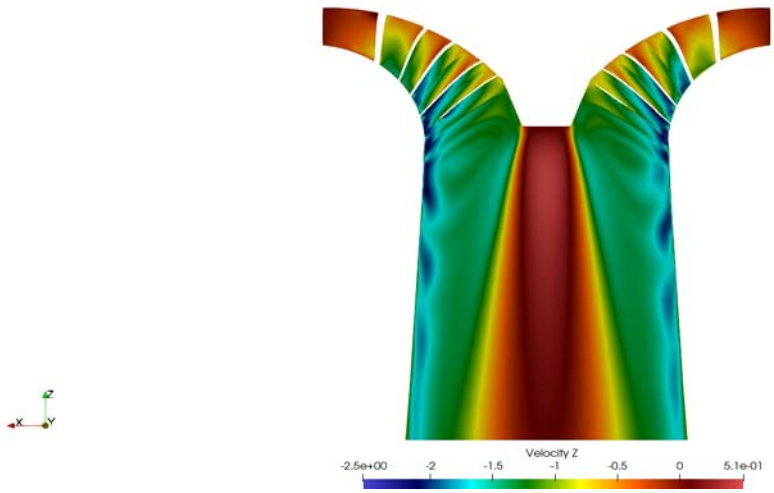

c)

Figure 4.3. Steady-state axial velocity, Frozen Rotor simulations c) PL.

At all operating regimes both the magnitude of velocity and axial velocity fields exhibits an axis-symmetric characteristic. At the PL operating regime, a broad recirculation zone extends over a substantial portion of the draft tube cone. This suggests the emergence of a substantial vortex, a phenomenon associated with vortex breakdown, which is characterized by a noteworthy residual swirl, as expounded upon in Chapter I.

4.5. RESULTS FOR FULL DRAFT TUBE GEOMETRY

An instantaneous screenshot of the pressure at the end of the unsteady-state simulations in shown in Figure 4.4 for the PL operating regime

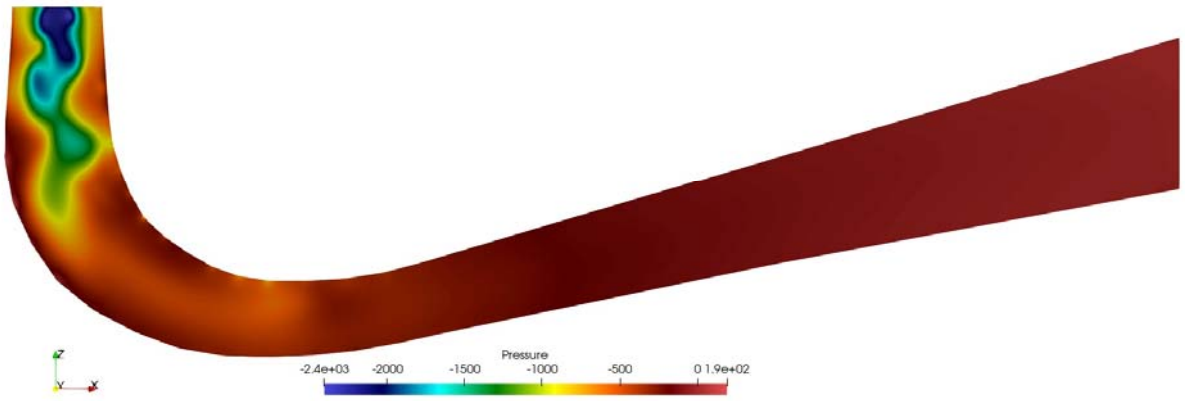

c)

Figure 4.4. Instant pressure at the end of simulation for c) PL.

On the other hand, the vortex development during the PL operating regime presents a strong rotational movement and it constantly flaps between the walls of the draft tube (Figure 4.5). This vortex, called the Rotating Vortex Rope (RVR) is observed to be rotating in the same direction as the runner rotational direction. The vortices observed under the Best Efficiency Point (BEP) and High Load (HL) operating conditions do not exhibit significant distinctive rotational features. As a result, it is relatively straightforward to time-average the velocity profiles and compare them with experimental data for validation purposes. However, due to the pronounced periodical and rotational nature of the Rotating Vortex Rope (RVR), the data saved using the monitoring point DT5 is essential to precisely determine the initiation period and frequency of the RVR. This approach ensures that the flow data is time-averaged over complete cycles of the RVR, providing a more accurate representation of its behavior.

c)

Figure 4.5. Spatial structure of the vortical structure – instantaneous screenshot at the end of the numerical simulation for c) PL.

Although the RVR is forming inside the draft tube after approximately 2 seconds of "physical" time, the pressure acquired in the monitoring point DT5 reveals that the RVR becomes truly periodical after approximately 9.6 seconds. Until then, although is fully developed after approximately 3 seconds after the beginning of the numerical simulation, strong pressure fluctuations are observed as it shown in the pressure in time plot from Figure 4.6.

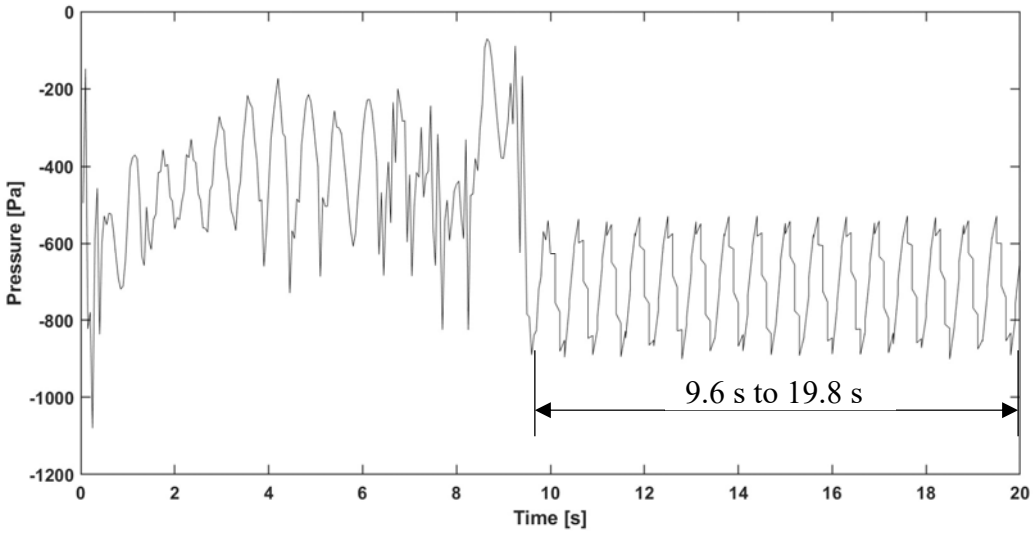

Figure 4.6. Pressure evolution in time – monitored in DT5 for PL regime.

A Fast Fourier Transform (FFT) is applied on the time interval from 9.6 s to 19.8 s, more exactly over 17 full RVR rotations in order to find the RVR frequency. The FFT analysis reveals a numerical frequency of the RVR, f_{RVR} = 1.56 Hz as shown in Figure 4.7.

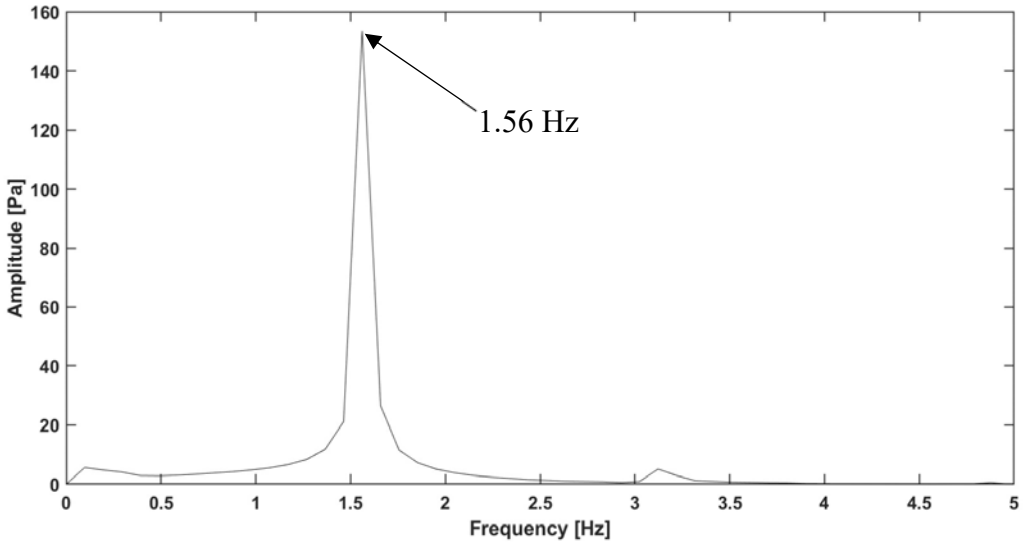

Figure 4.7. Numerical fr

equency of the RVR, f_{RVR} = 1.56 Hz.

Considering the frequency of the runner f_{runner} = 5.55 Hz, it means that the numerical frequency of the RVR is approximately $f_{RVR} = 0.28 f_{runner}$ [86]. This result is confirmed by other research studies [85] that found that the frequency of the RVR is in the interval 0.2-0.4 of the runner frequency [19]. Moreover, the experimental frequency of the RVR revealed from the FFT applied to the experimental pressure data is determined to be f_{RVRExp} = 1.6 Hz, which compared to the numerical one of f_{RVR} = 1.56 Hz, results in an evaluation error between the numerical and experimental of ~2.5 %.

4.6. CONCLUSIONS

The chapter presents the results of the numerical simulations of the flow inside the draft tube of a laboratory model of a Francis hydraulic turbine using RANS models with *k-ε* turbulence models. The numerical simulations are carried out for the BEP and for the off-design operating regimes, HL and, respectively, PL operating regime. To reduce the computational costs, including the computational time, numerical simulations are performed consequently on simplified geometries instead of using the entire hydraulic scheme. First, the numerical simulations are carried out in a simplified geometry consisting in a runner passage and a part of the draft tube. In this case a steady-state flow algorithm is used accompanied by a Frozen Rotor Turbomachinery model. The Frozen Rotor Turbomachinery provides the possibility to impose a rotational velocity to a part of the numerical model simulating therefore a rotational movement. Although some remarks may be done by analyzing the flow distribution regarding the recirculation zones and possible apparition of a vortical flow it is not enough to solve the unsteady character of the flow inside a turbine draft tube and to provide relevant information.

The velocity profiles are extracted from the zone corresponding to the inlet of the draft tube and used as boundary conditions on the inlet of a full draft tube geometry. The time-averaged profiles of the velocities are compared to the time-averaged velocities obtained during the measurement campaigns. The best results for both axial and radial components are at the BEP operating regime. When sliding to off-design operating points, the axial velocity follows the trend of the experimental values but the at the PL regime it tends to be underestimated in the middle of the draft tube cone. At HL and PL operating regime, the radial velocity profiles are slightly different from the experimental data. Similar results are also reported in literature leading to the idea that due to the high magnitude order of difference between the radial and tangential velocities, the measurement tools could not acquire the radial velocity with the desire accuracy.

5. FLOW AROUND A CIRCULAR BLUFF-BODY

5.1. FLOW CONFIGURATION AND PROBLEM FORMULATION

The numerical simulations are performed for six values of the Reynolds numbers, respectively 60, 80, 100, 120, 140 and 160 and compared to the data available in the literature. Both the steady state and the unsteady state solutions are computed for each value of the Reynolds number. In the steady state case, the partial derivative in respect to the time t is eliminated as the solution of such case is time independent, i.e. the flow does not vary with time. In the unsteady state case, the flow is dependent on the time, so a time step of $\Delta t = 0.05$ non- dimensional time units is chosen for the cases where Reynold number ranges from 60 to 80 and the numerical simulations are carried out with a maximum iteration number of 12000. This means that the flow is analyzed over a period of 600 non-dimensional time units. On the other hand, when Re ranges from 100 to 160, a lower time step of $\Delta t = 0.025$ non-dimensional time units is chosen to ensure a proper convergence and stability to the numerical simulation. To analyze the flow over a period of 600 non-dimensional time units, the number of iterations is increased to 24000.

A monitoring point P1 is added just off-axis behind/downstream the circular bluff body at the coordinates of $(x, y) = (2.5, 0.5)$ to acquire the essential data about the velocity and pressure evolution.

5.2. RESULTS

To fasten the convergence in the unsteady-state simulations, the steady-state flow solutions are initially employed as an initialization, and thus, the discussion begins with the steady-state simulations. At last, it is mentioned that the *post-processing* part is performed using Matlab [92] and Paraview [93].

5.2.1. **Steady-State case**

It is recalled from the Numerical Method chapter that the steady-state flow is calculated using a conventional Newton-Raphson algorithm. This iterative approach solves the governing equations assuming there is an initial estimate for the flow solution that approximately complies with the governing equations. In each iteration, it progressively introduces a corrective term until the results reach a predefined residual threshold. For the current thesis, the residuals are set to a minimum of 10^{-6} and, as an additional measure, a maximum number of 100 iterations is set. In other words, if after 100 iterations the residuals are still higher than the minimum value, the numerical simulations ends. However it was not the case, as all test cases converged after 7-8 iterations. For convenience, all the initial estimated values for the axial and radial velocity components, respectively for the pressure are set to a null value. In Figure 5.1 it is shown as an example the steady-state streamwise velocity for two different values of Re = 80 and 100.

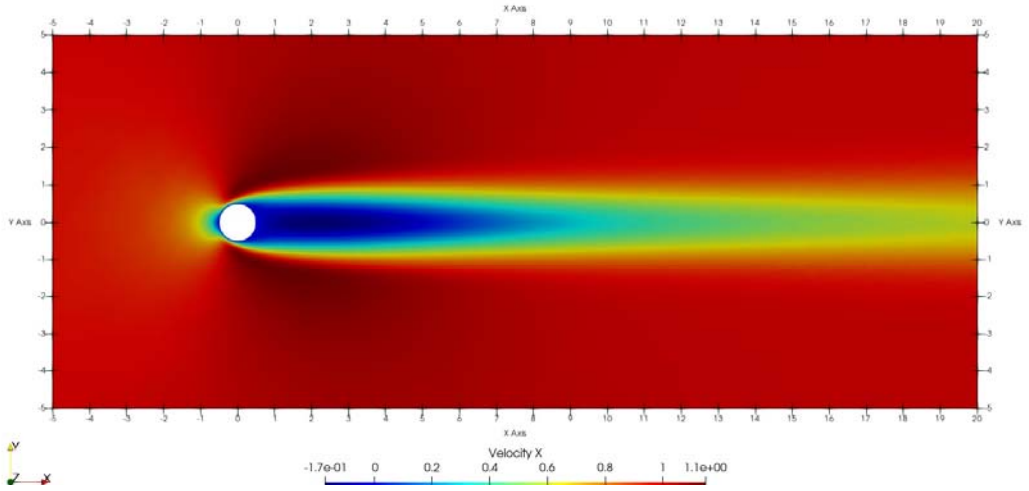

b)

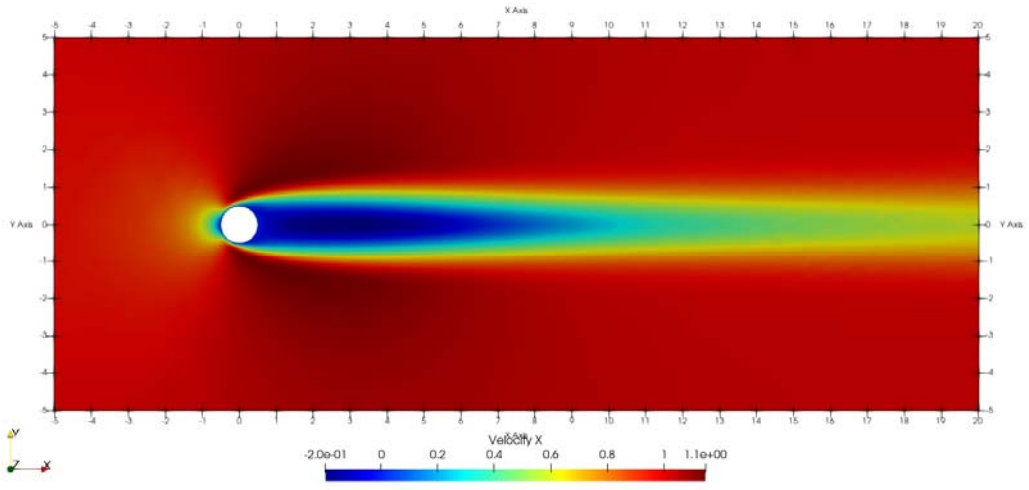

c)

Figure 5.1. Stream-wise component of the velocity, from top to bottom, at Re = 80, 100.

5.2.2. Unsteady-state case

To determine the non-dimensional frequency of the vortex shedding, denoted as the Strouhal number, a Fast Fourier Transform of the axial velocity is applied over a period spanning 30 complete fully developed vortex shedding cycles (Figure 5.2). The FFT analysis is presented in Figure 5.3.

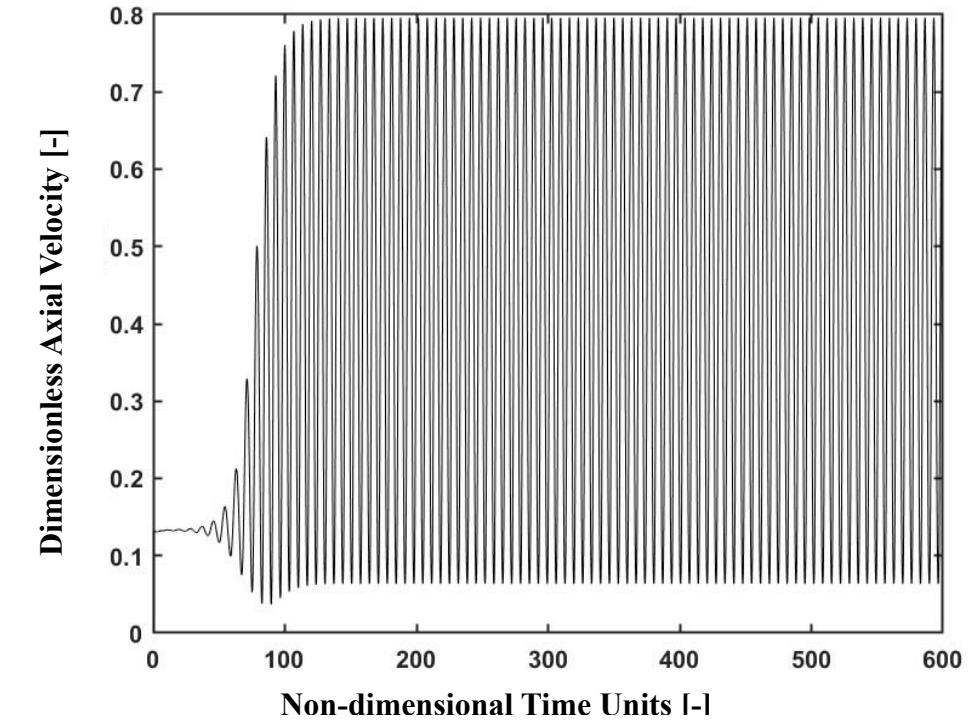

b)

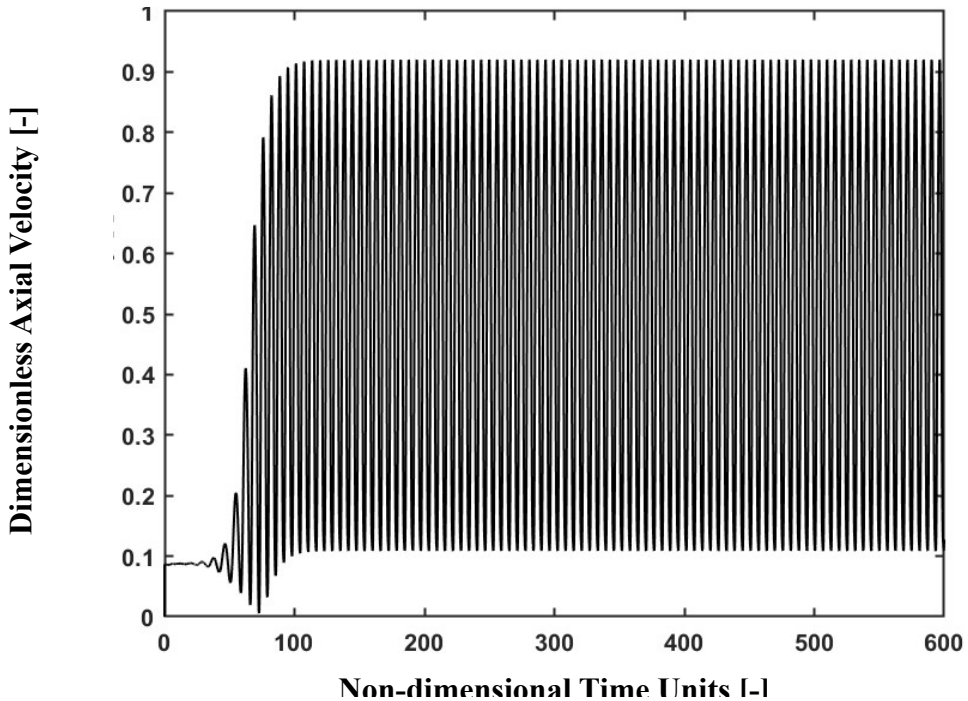

c)

Figure 5.2. Axial velocity evolution monitored in P1 for different Reynolds number values b) 80, c) 100.

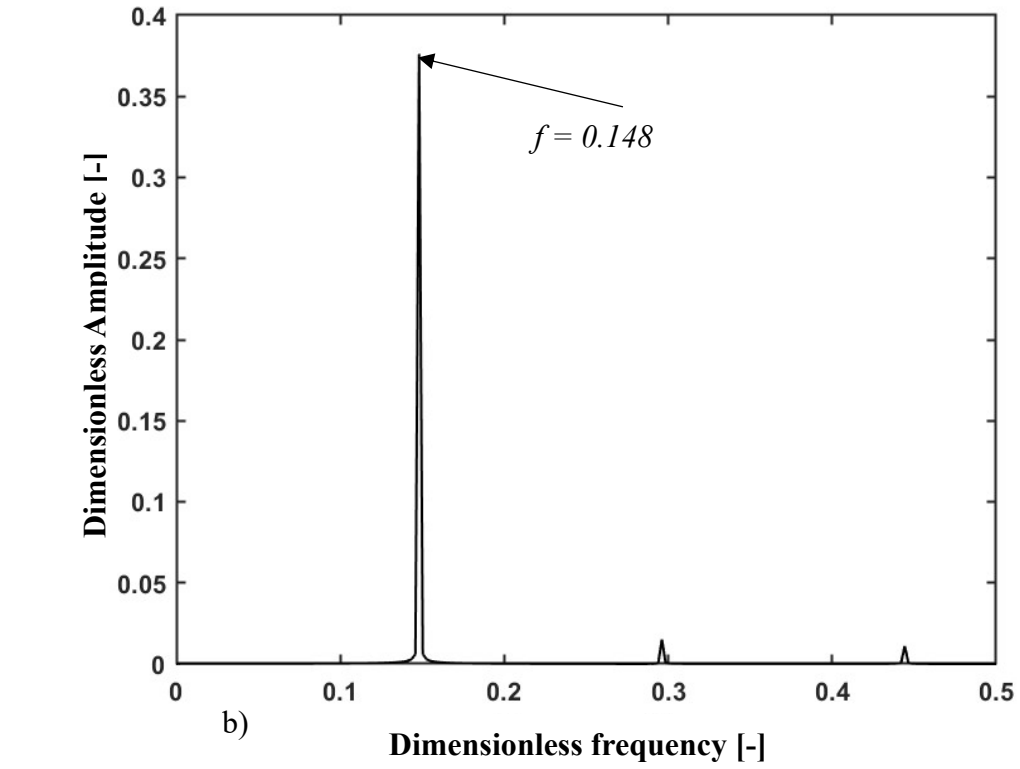

b)

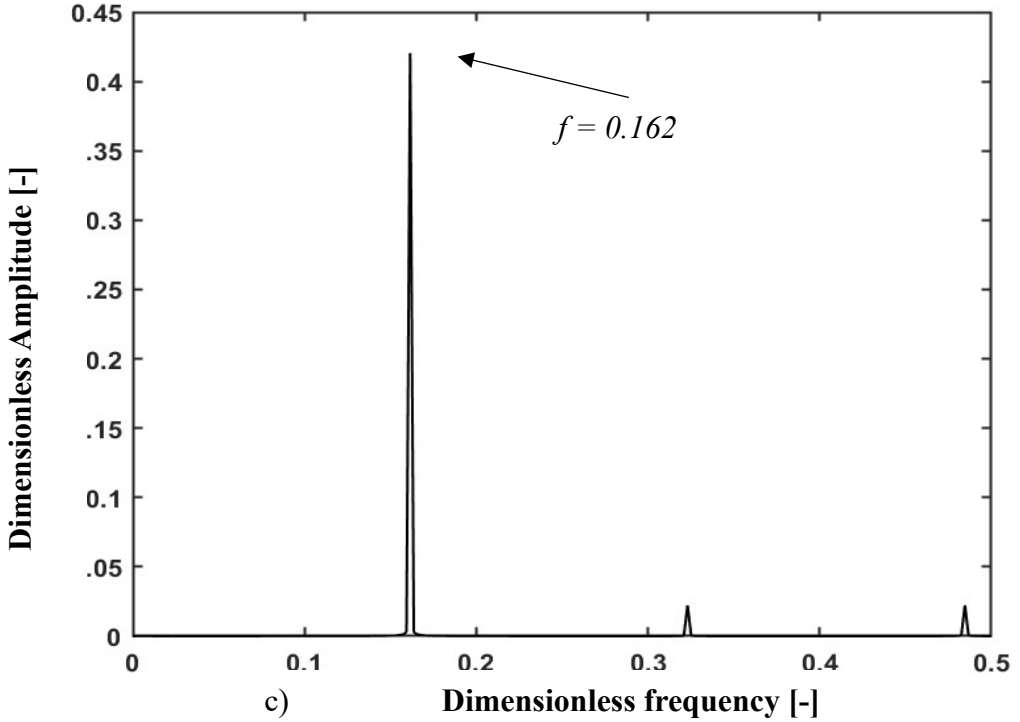

c)

Figure 5.3. Non-dimensional frequency of the vortex shedding at different Reynolds number values 60, b) 80, c) 100.

The same principle applied to the FFT methodology is considered when time-averaging the axial velocity. The time-averaged velocity for each case is shown in Figure 5.4

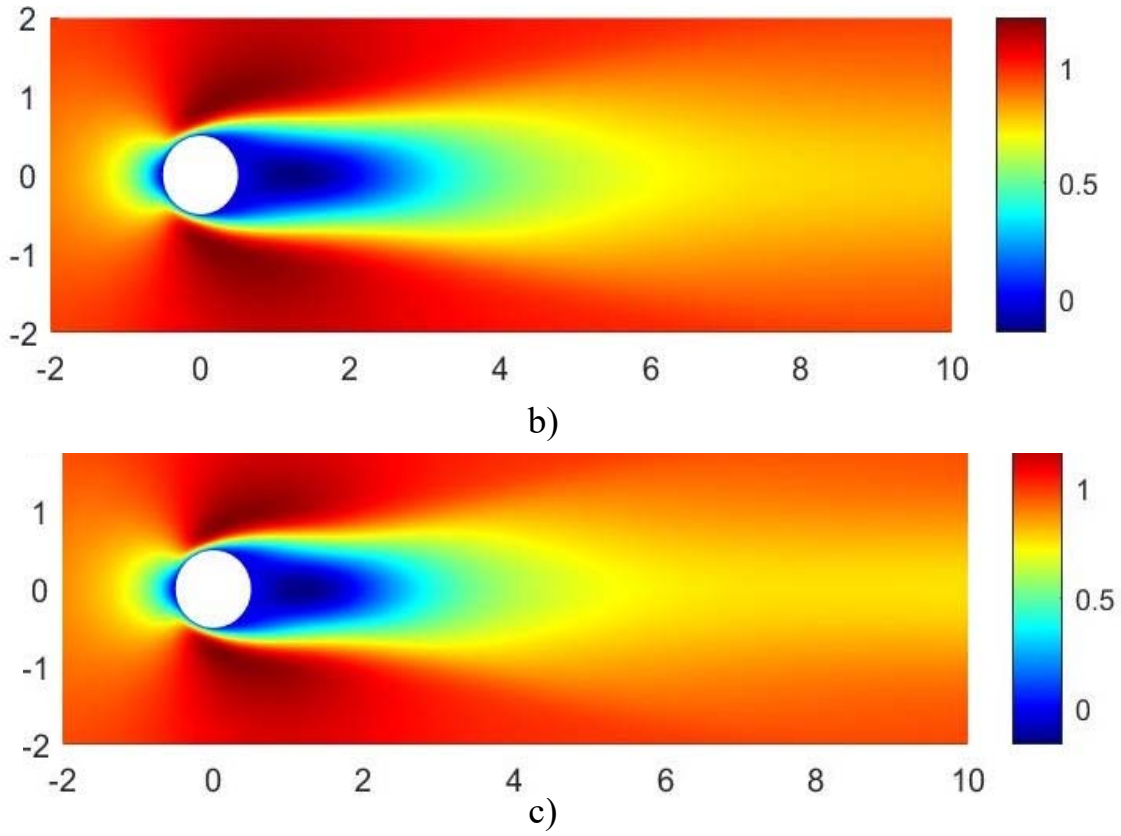

Figure 5.4 Mean axial velocity for different Reynolds number values b) 80, c) 100.

It is interesting to see that opposite to the steady-state flow solution, the mean flow presents a significantly lower recirculation zone, fact confirmed by the streamlines plot shown in Figure 5.5. This could be attributed to the fact that the time-averaging smooths out the fluctuations in the flow, including the ones associated with the vortex shedding.

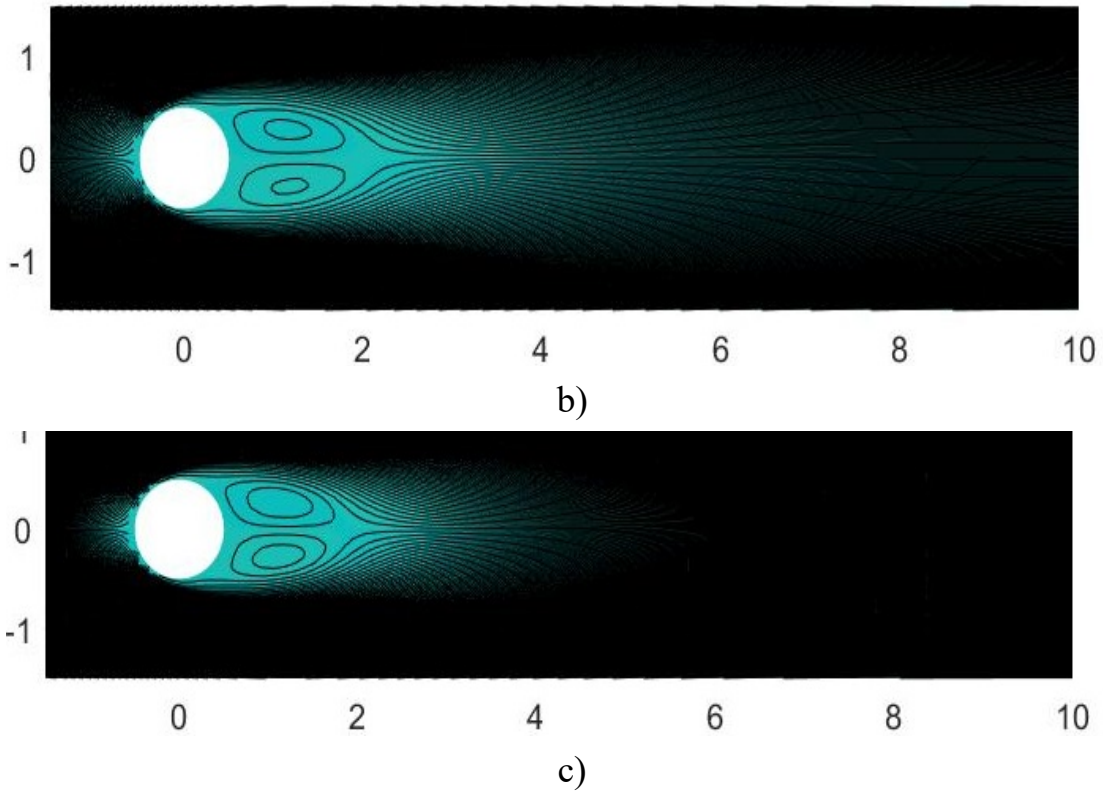

Figure 5.5 Mean axial velocity stream lines for different Reynolds number values b) 80, c) 100.

5.3. CONCLUSIONS

The current chapter investigates the dynamics of laminar fluid flow around a circular bluff body, for Reynolds numbers within the range of 60 to 160. The governing equations and the numerical methods detailed in the previous chapters are put to practical test through the utilization of the FreeFEM++ numerical software. In preparation for Linear Global Stability Analysis, both steady-state and unsteady-state flow solutions are acquired for various flow regimes.

Once an optimal *mesh* is achieved, steady-state flow computations are conducted. For validation purposes, a commonly testcase as the flow around a circular body is used, to examine the recirculation length in the bluff body wake, demonstrating close alignment with literature data. The flow around a bluff body leads to boundary separation and eventually to periodical vortex shedding. Analyzing this periodic phenomenon necessitates the acquisition of unsteady-state flow solutions.

Over the same interval, the flow is time-averaged and the recirculation zone appearing behind the circular cylinder is compared to the one from the steady-state simulations. It is observed that the time-averaging procedure attenuates the pressure gradients, therefore the recirculation lengths are significantly smaller than the ones from the steady-state simulations. In the steady-state scenarios, an increase in Reynolds number corresponds to an increase in recirculation lengths. However, in the mean flow analysis, higher Reynolds numbers result in greater attenuation, causing the recirculation length to decrease.

6. TWO-DIMENSIONAL STABILITY ANALYSIS OF THE WAKE DOWNSTREAM A CYLINDER

Chapter 6 aims to investigate the results presented in Chapter 5 under the perspective of a Linear Global Stability Analysis (LGSA) derived in Chapter 2 using the numerical methods presented in Chapter 3.

Both the flow around a bluff-body and the flow inside hydraulic turbines belong to the open flows category, meaning that the fluid particles continuously enter and leave the studied domain. As shown in the results from Chapter 4 and Chapter 5, in both configurations the flow presents similarities such as the recirculation zones, in the wake of the bluff-body, respectively under the runner hub in the hydraulic draft tube case. Furthermore, in both scenarios, it is observed the presence of a synchronized periodical self-sustained oscillations. These self-sustained oscillations develop in open flow when an external infinitesimal disturbance enters the system and grows in space and time leading to an unstable system which saturates to a limit-cycle state [94]. Therefore, the flow field becomes unstable behaving like a global oscillator and the spatial structure of the leading unstable perturbation is called an unstable global eigenmode.

To justify the numerical simulation performed in both steady-state and unsteady-state case it is brought in discussion the difference between the LGSA of the steady-state flow solution and of the mean flow solution. As remarked by Barkley [32], the LGSA of the steady-

state flow solution captures the frequency of the vortex shedding in the immediately vicinity of the critical Reynolds number where the Hopf bifurcation occurs. As there is not yet a reason globally accepted for the sudden decrease in the frequency revealed by the LGSA that observed when moving away from this critical point, the growth rate of the instability is however correctly captured. On the other hand, the LGSA of the mean flow offers a better consideration of the nonlinear effects and consequently of the saturation mechanism of the flow oscillations resulting a precise outcome of their frequency. In the same time, it is observed that due to the Reynolds stresses that induce a distortion of the mean flow, the growth rate of the perturbation is incorrectly captured and it usually revolves around null values [36], [97], [98].

6.1. RESULTS

The presented data includes the results obtained from LGSA of both steady-state flow and mean flow solutions. It is worth noting that the imaginary part calculated using FreeFEM++ software corresponds to an angular frequency. To obtain the non-dimensional frequencies of the instabilities as presented in this thesis, the imaginary parts, i.e. the angular frequencies, are divided by 2π. Additionally, it is important to mention that only the real part of the eigenmodes is shown in the current thesis.

6.1.1. **LGSA of mean flow solution**

Figure 6.1. shows the real part of the direct eigenmodes of the axial velocity perturbation component. The spatial structures of the eigenmodes develop downstream of the circular bluff-body and does not change considerably when the Reynolds number increases. The maximum intensity peaks are observed to occur close to the recirculation area. When the Reynolds number increases, the maximum intensity peaks are observed to decay after a longer distance each time, almost proportionally with the recirculation lengths L_x, in the wake of the circular bluff-body.

The real part of the adjoint eigenmodes of the axial velocity perturbation component presents a strong contrast in the spatial structures compared to the direct eigenmodes. In this case the maximum receptivity is shown to be in the immediately vicinity of the bluff-body, close to its upper and lower sides.

The real part of the direct eigenmodes of the axial velocity perturbation component are shown in Figure 6.2. It is immediately observed that the eigenmode vanishes much faster than eigenmodes computed using the mean flow. The real part of the adjoint eigenmodes of the axial velocity perturbation component are shown in Figure 6.2

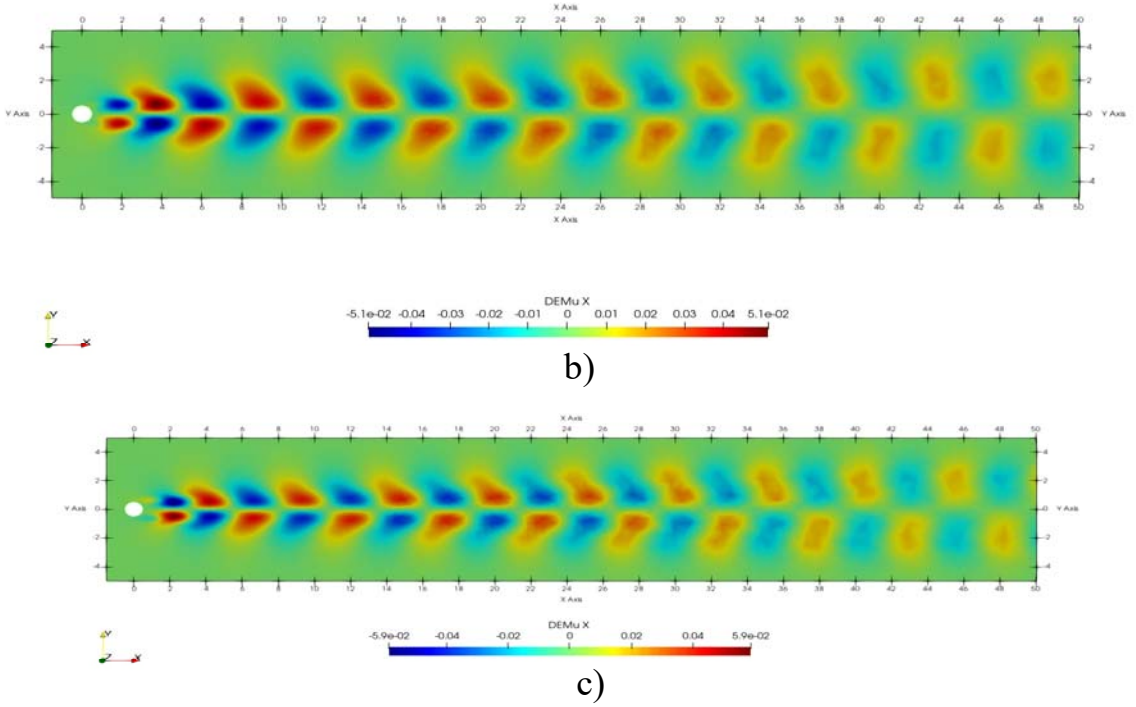

Figure 6.1. The real part of the direct eigenmodes of the axial velocity perturbation component, at different values of the Reynolds number, in mean flow stability analysis: b) 80, c) 100.

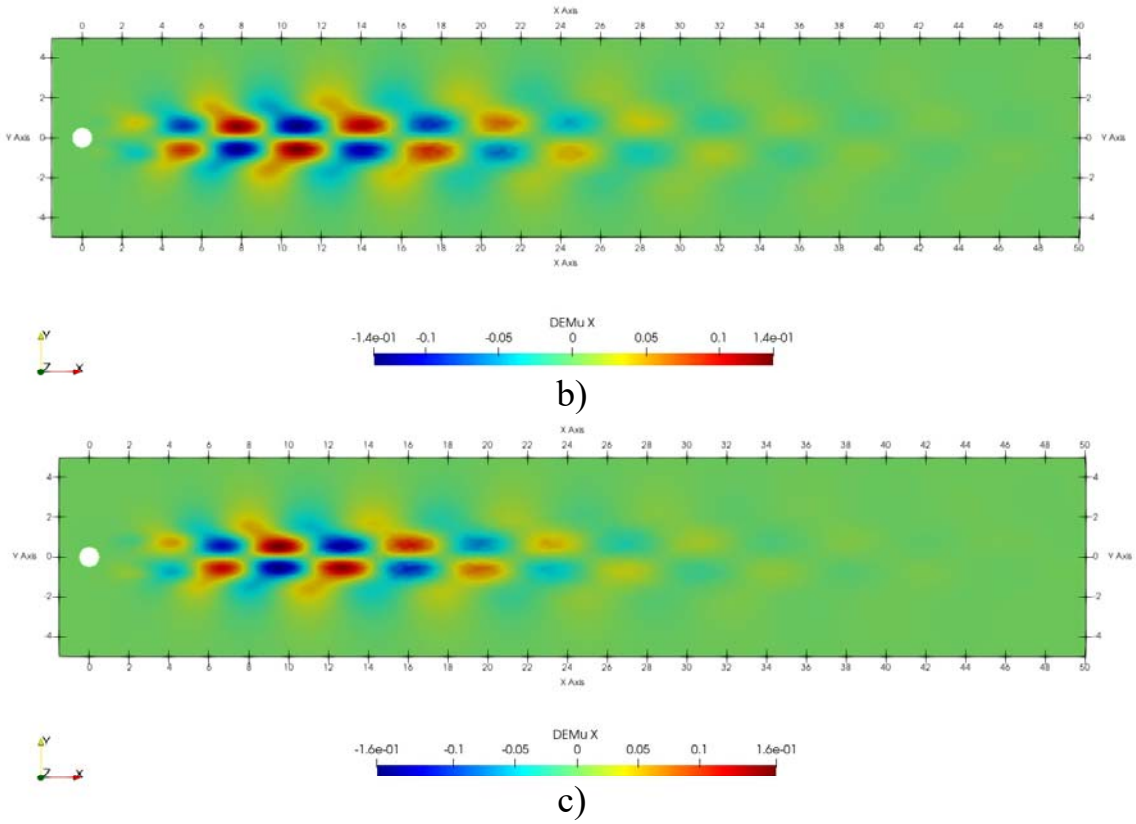

Figure 6.2. The real part of the direct eigenmodes of the axial velocity perturbation component at different values of the Reynolds numbers in steady-state flow stability analysis: b) 80, c) 100.

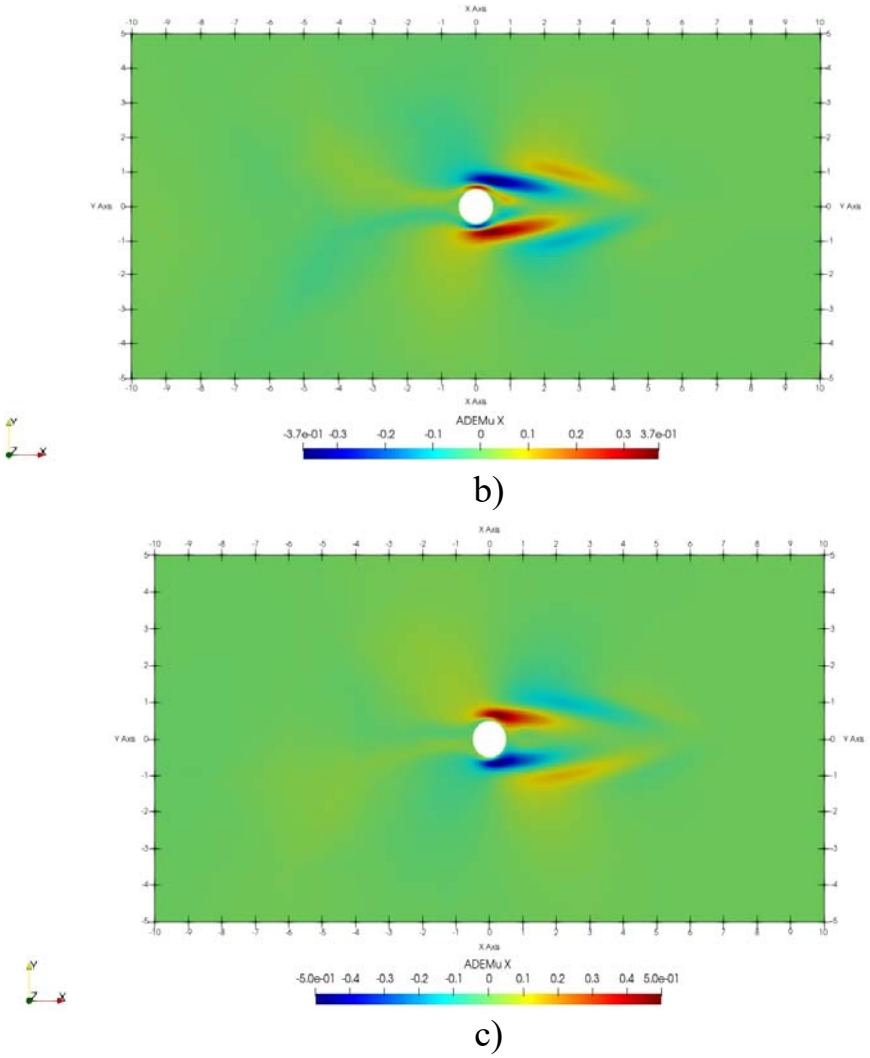

Figure 6.3. Axial velocity component, adjoint eigenmodes at different values of the Reynolds number in steady-state flow stability analysis: b) 80, c) 100.

6.2. STRUCTURAL SENSITIVITY OF THE STEADY-STATE FLOW

The significant spatial differences between the direct and adjoint spatial structures suggest that the underlaying mechanism which triggers the apparition of the instabilities cannot be identified by studying the eigenfunctions in separate instances. The maximum values of the structural sensitivity tensor, determines the *wavemaker* region. Therefore, the velocity components of the perturbations may be used to determine the locations where the instability mechanism has the highest intensity. In other words, the *wavemaker* region is a spatial location where a modification in the flow structure induces the most substantial drift in the eigenvalue. In such circumstances, it is justified to consider that this modification must be placed in the core of the instability mechanism. In the current thesis the *wavemaker* region is determined for different values of the Reynolds number in the structural sensitivity maps, as it is presented in Figure 6.4.

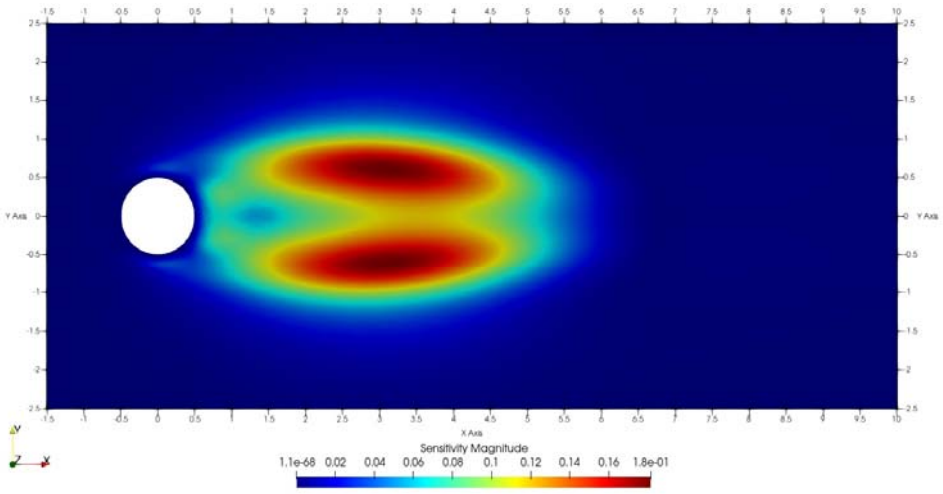

b)

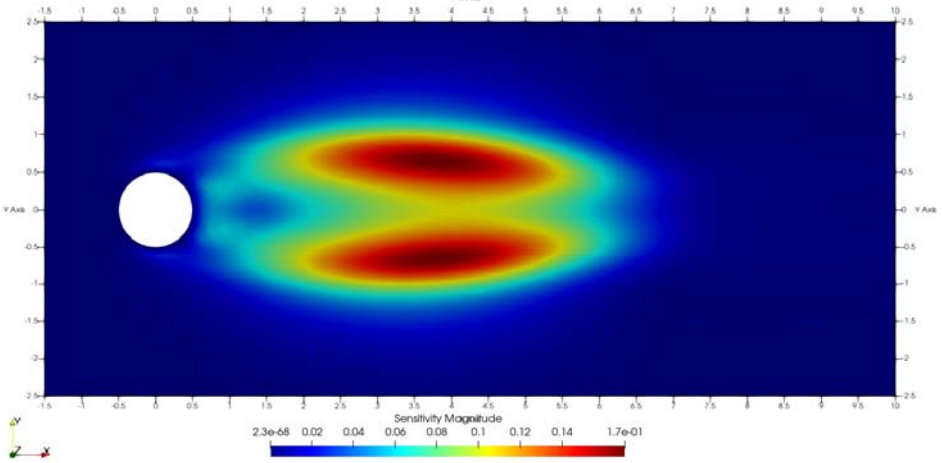

c)

Figure 6.4. Structural sensitivity maps with the *wavemaker* region at different values of the Reynolds number b) 80, c) 100.

In Figure 6.4, it is seen that in both the immediate vicinity of the circular bluff-body and at a considerable distance from it, the norm of the structural sensitivity tensor, S_w, calculated with equation. (2.7) which combines the direct and adjoint eigenmodes is exceptionally low, approaching zero. This observation implies that these particular regions within the flow do not hold significant importance when investigating instability dynamics. It's worth emphasizing that the spatial structure of both the direct and adjoint eigenmodes typically exhibits their highest intensity in these less significant zones. This highlights the necessity of studying them in conjunction with each other.

Once the most receptive zones are determined, small control bluff-bodies of different shapes and dimensions are inserted into those areas. In the current thesis it will be investigated the modification of the steady-state flow at Re = 80 by placing in the *wavemaker* region three different bluff-bodies: a small cylinder with a diameter of $d = 0.1D$ and an elliptical shape with an aspect-ratio of the major-to-minor axis of 3, where the major axis has a length of $3D$ and the minor axis has a length of $1D$. These shapes are in both lobes of the *wavemaker* region as shown in Figure 6.5.

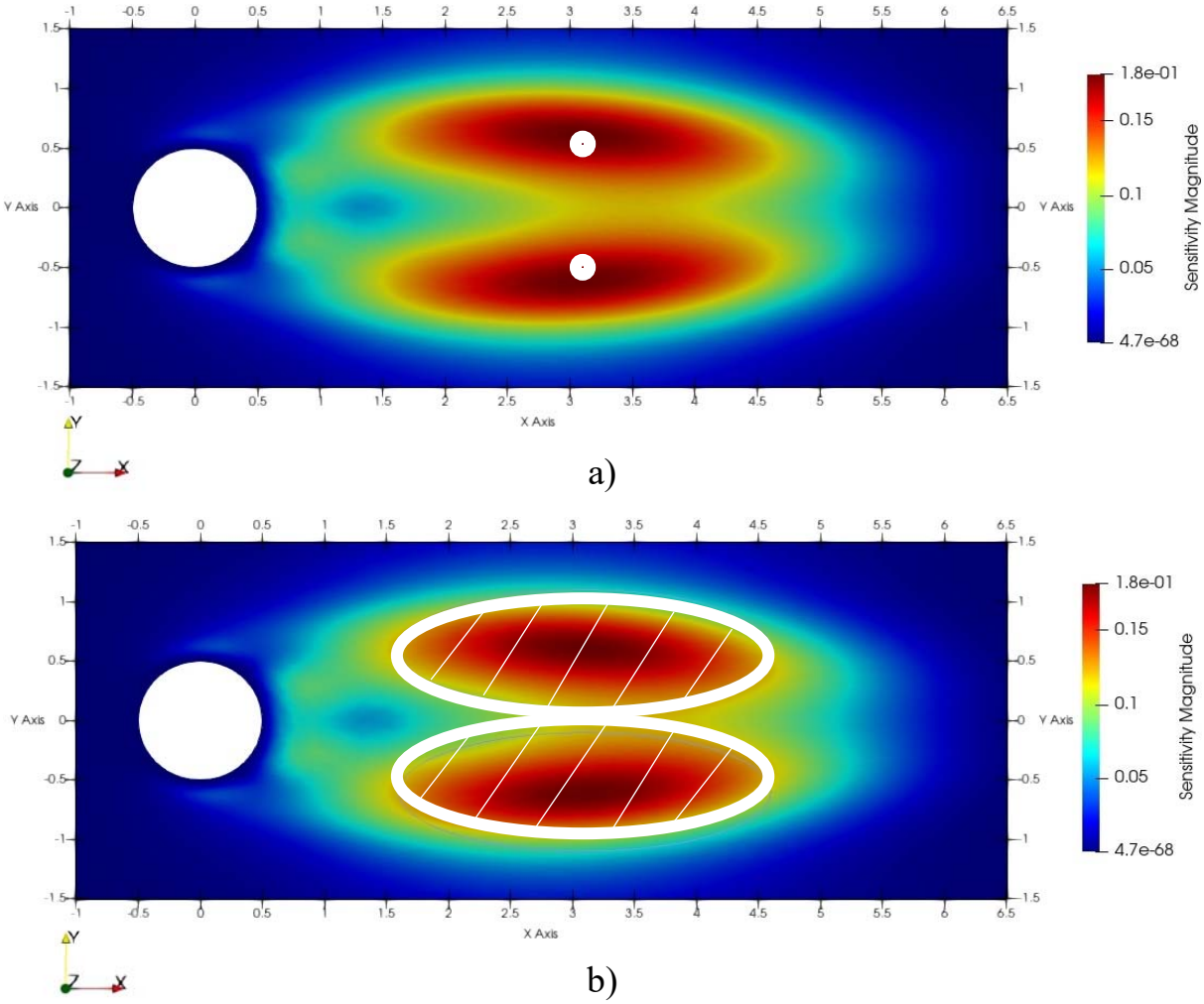

Figure 6.5. Control bluff-bodies placement a) two small cylinder of 0.1D diameter, b) two elliptical shapes with size ratio of 1D/3D.

The eigenvalue computation reveals that the two small control circular bluff-bodies placed in both lobes of the *wavemaker* are not enough to mitigate the onset of the instabilities as the leading eigenvalue has a value of ω_{cc}= *0.072 + i0.72*. This is however a diminution by ~29.17% of the growth rate compared to the case with no control bluff-bodies.

The first ten most unstable eigenvalues computed for both cases is shown in Figure 6.6. The two elliptical shapes covering entirely both lobes of the *wavemaker* region successfully mitigated the instability by reducing the growth rates to negative values which means that in this case the flow becomes linearly stable [32]. The growth rates of the leading eigenvalues are centralized in Table 6.1 where C1 stands for the case without control bluff-bodies, C2 stands for the case with two control cylinders of *d = 0.1D* and C3 stands for the case with two control elliptical shaped bluff-bodies.

Table 6.1 Growth rates of the leading eigenvalues for Re = 80 without and with control bluff-bodies

Re = 80	C1	C2	C3
Growth Rates	0.093	0.072	-0.049

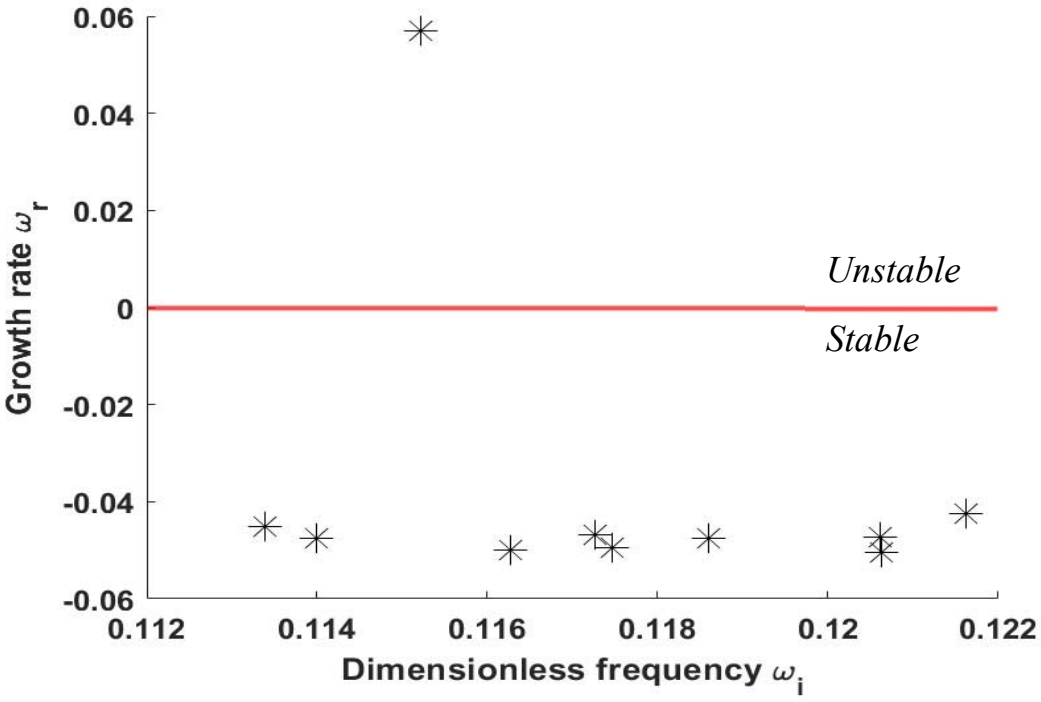

a)

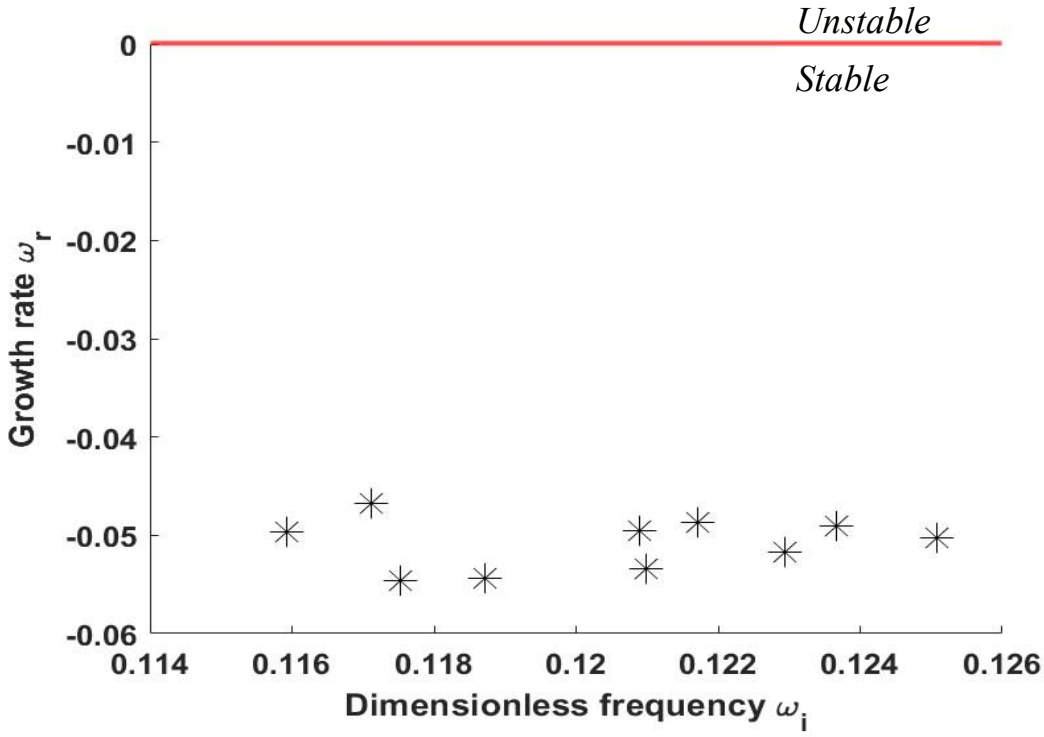

b)

Figure 6.6. Eigenvalues computed at Re = 80, a) two small cylinder of 0.1*D* diameter, b) two elliptical shapes with size ratio of 1*D*/3*D*.

6.3. CONCLUSIONS

To test the theory, the test case for Re = 80 is arbitrary chosen for further investigation. Various bluff-bodies, each with distinct shapes and lengths, are placed within the symmetrical lobes. Subsequently, Linear Global Stability Analysis (LGSA) is conducted to monitor the evolution of growth rates. It is immediately observed that by placing small control bluff-bodies in the wake of the main bluff-body the growth rates are reduced. By placing two small cylinders of diameter 10 times smaller than the main bluff-body diameter, i.e. $d=0.1D$, the growth rate is reduced by approximately 29 %. By placing two elliptical shapes, each covering entirely the lobes shown in the sensitivity maps, the flow is linearly stabilized as the LGSA returns only negative values of the growth rate.

7. CONCLUSIONS AND FUTURE WORK

By identifying the onset region of these instabilities or the exact location where an external force may be applied in order to mitigate them, practical methods could be developed in order to prevent the apparition of the RVR.

First, numerical studies are carried out for turbulent flows inside a hydraulic turbine draft tube operating at the BEP, HL and PL. The analysis was performed for two geometries: a full turbine draft tube and a reduced geometry of a hydraulic turbine runner passage and a part of the draft tube. Second, numerical studies are carried out to study the dynamics of a flow obscured by a bluff-body at different values of the Reynolds number. In the end, the location of additional bluff-bodies is investigated in order to reduce or even eliminate the flow instability in the vicinity of the main bluff-body.

Additional objectives reached in the current thesis are:

- the use of open-source, free CFD software, Code_Saturne to perform 3D numerical simulations of the flow in a simplified geometry using periodical boundaries and in a complete geometry of a draft tube;
- to perform steady-state numerical simulations using the turbomachinery module, Frozen Rotor of the Code_Saturne to simulate the rotation of the runner;
- to perform unsteady-state numerical simulations of the flow inside the draft tube of a hydraulic turbine using RANS with k-ε turbulence model;
- the use of open-source, CAD software, Salome to improve the quality of existing meshes through its mesh module, SMESH;
- the use of open-source, free CFD software, FreeFEM++ to perform 2D numerical simulations of a flow around a bluff-body, perform stability analysis of a 2D flow around a bluff-body and to compute sensitivity maps of a 2D flow around a bluff-body. Additionally, its functions are used to create Finite Element Meshes for the numerical analysis.
- to validate the results with experimental data available in the scientific literature.

7.1. GENERAL CONCLUSIONS

The vortex occurring at PL presents a strong rotational movement and it is observed to rotate in the same direction as the runner. The flow is time-averaged and the resulted mean flows are compared with the mean flows obtained from the experimental data. Overall, in all cases the numerical values of the velocities follow the trend of the experimental velocities, with small deviations

Using the pressure monitored during the numerical simulations, a Fast Fourier Transform (FFT) is applied to the pressure to determine the frequency of the RVR which is observed to appear during the PL operating regime. The numerical frequency of the RVR is found to be 1.56 Hz, f_{RVR} = 1.56 Hz. Using the experimental values provided in [81], the experimental frequency of the RVR is 1.6 Hz, , f_{ExpRVR} = 1.6 Hz. Therefore, the error between the numerical and experimental frequency is of an acceptable value of ~2.5 %.

An effective way to investigate the dynamics of the RVR is to employ simplified flow setups that resemble the RVR. The flow in hydraulic turbines belongs to the category of open flows and so is the flow around bluff-bodies. Therefore, numerical simulations of the two-dimensional flow around a circular bluff-body using a laminar incompressible flow are performed at different Reynolds number values of 60, 80, 100, 120, 140 and 160 using the FreeFEM++ software. This open-source software is based on the Finite Element Method, thus before performing the numerical simulations, the governing equations must be linearized according to the theory. Moreover, the purpose of these studies is to understand the underlaying phenomenon which leads to the apparition of the vortex shedding, so a Linear Global Stability Analysis (LGSA) is performed at each Reynolds number. The LGSA equations are determined by inserting a small external infinitesimal perturbation into the flow and its spatial-temporal evolution is studied by the means of a modal analysis. The LGSA equations represent in fact an EigenValue problem (EVP).

The steady-state numerical simulations of the flow around a circular bluff-body reveal the presence of recirculation zones downstream the bluff-bodies similar to the recirculation zones presented in the case of the flow inside the draft tube. These recirculation zones are observed to increase when the Reynolds number becomes higher due to the steeper pressure gradient which intensifies the flow separation from its surface. The length of the recirculation zone is compared with available data in the literature for validation purposes [35]. The steady-state results are used as initialization for unsteady-state numerical simulations of the flow around the circular bluff-body to ensure a fasten convergence. A monitoring point is added downstream of the circular bluff-body just off-axis to monitor the evolution of the pressure and axial velocity in time. Plotting the axial velocity evolution in time allows to observe the evolution of the vortex shedding. Once the vortex shedding is observed to become periodically, the axial velocity over a period of 50 fully developed vortex shedding cycles is used to perform Fast Fourier Transform (FFT) analyses. The frequency of the vortex shedding obtained from the FFT is compared with the available data in literature for validation purposes [35]. Further, the flow is time-averaged over the same period chosen for the FFT analysis resulting in the mean flow. Notably, the time-averaging process diminishes the impact of pressure gradients, leading to considerably shorter recirculation lengths compared to those observed in steady-state simulations. Conversely, within the context of mean flow analysis, higher Reynolds numbers

lead to more pronounced attenuation, resulting in a reduction of the recirculation length compared to the steady-state flows.

Once the steady-state flows and mean flows are obtained from the previous numerical simulations, the LGSA is carried out for both of them. The LGSA of the steady-state flow is observed to capture well the growth rate values of the instabilities but the frequency prediction of the instabilities is far from the reality, facts confirmed also in the literature [32]. On the other hand, the LGSA of the mean flow offers a very good prediction of the frequency of the instabilities but it fails to capture the growth rates. In this case, the growth rates are around a null value, indicating the necessity of using an extended mean flow analysis as the flow presents marginally stable characteristics. The real part of the direct eigenmodes of the axial velocity perturbation components are plotted considering the both direct and adjoint scenarios of the LGSA of the steady-state and mean flow cases. Within the framework of steady-state flow, it is observed that the direct eigenmodes of the axial velocity perturbation component initially emerge in the proximity to the bluff-body at lower Reynolds numbers and travel a relatively short distance downstream. As the Reynolds number increases, these direct eigenmodes shift their development further downstream, away from the bluff-body, and exhibit a shorter developmental trajectory. In contrast, in the case of adjoint eigenmodes of the axial velocity perturbation component within the steady-state flow, they tend to develop near both the upper and lower sides of the bluff-body and upstream of the circular bluff-body. Similarly, patterns are observed in the adjoint eigenmodes of the axial velocity perturbation component of mean flow, with differences primarily found in their intensity. Conversely, direct eigenmodes of the axial velocity perturbation component in mean flow tend to develop right after the bluff-body in its wake, and the Reynolds number does not seem to significantly affect the development of the eigenmode. Instead, a longer and more intense path is observed. One distinction between the direct eigenmodes of steady-state flow and mean flow lies in their spatial structure. In the latter case, the spatial structure appears to extend all the way to the end of the computational domain. Due to the significant difference between the direct and adjoint eigenmodes a structural sensitivity analysis involving the dot product of them is necessary to find the most receptive zone in the flow to an external force which may modify its stability properties. In the current thesis it is aimed to bring the flow to a linearly stable condition, i.e. bring the growth rates to negative values. Considering the results of the LGSA of the steady-state flow which indicate a good growth rate prediction, the sensitivity analysis is not performed using the mean flow too.

The sensitivity analysis reveals for all Reynolds number studied cases two axisymmetric lobes with peak intensity emerging in the wake of the bluff body. In other areas, the intensity tends to approach minimal values. This observation suggests that relying on an individual analysis of direct or adjoint stability properties may not be a practical strategy for controlling and mitigating instabilities. With increasing Reynolds numbers, in the sensitivity maps the *wavemaker* region tends to originate at greater distances from the bluff body and exhibit elongated symmetrical lobes.

To test the theory, several additional control bluff-bodies of different shapes and sizes are strategically positioned in the core of the lobes indicated by the sensitivity analysis generated by the main bluff-body. The test case of the flow around the circular bluff-body at a Reynolds number of 80 is arbitrary chosen for this part. Subsequently, the LGSA is conducted to monitor the impact of placement of these distinct control bluff-bodies in the growth rates evolution. It is observed that by placing two small control circular bluff-bodies in both lobes, the growth rate

of the leading eigenvalue is decreased by 29%. Additionally, by placing two elliptical shapes each covering entirely the two lobes, the flow is linearly stabilized as the LGSA returns only negative growth rates.

7.2. PERSONAL CONTRIBUTIONS

The original contributions of the author are summarized among a set of guidelines are recommendations in the following points:

- The use of open CAD and CFD software for the numerical analysis, with good validation of the results against experimental data available in the literature
- Adjust the original meshes of the simplified runner and of the draft tube geometries to comply with the free open-source CFD software, Code_Saturne. The adjustments consist in the removing the internal faces which are seen as walls by the Code_Saturne, remove the runner hub from the draft tube inlet and level the inlet to a flat surface. The entire operation is performed using a free open-source CAD software, namely Salome through its SMESH module;
- Extract the velocity profiles on the draft tube inlet of the Francis-99 model turbine for each operating regime and implement them as boundary conditions. The implementation of such profiles requires the usage of the internal functions of the Code_Saturne and knowledge of the Fortran90 programming language is necessary;
- Perform numerical stability using the free open-source CFD software, the Code_Saturne only in the draft tube of the Francis-99 model turbine and validate the results with the experimental work with good accuracy (2.5% underestimation of the numerical frequency of the RVR compared to the experimental frequency);
- Create a two-dimensional finite element mesh using the free open-source FreeFEM++ adapted to the gradient of the axial velocity component of the vortex shedding flow downstream a circular bluff-body;
- Implement the *weak formulation* of the linearized Navier-Stokes equations, direct linear global stability analysis and adjoint linear global stability analysis equations into the free open-source FreeFEM++. This implementation requires the knowledge of the C++ language;
- Present the direct and adjoint eigenmodes of an unstable steady-state and unsteady-state flow solution around a circular bluff-bodies for different laminar Reynolds numbers, i.e. 60, 80, 100, 120, 140 and 160 computed using the free open-source FreeFEM++;
- Present the sensitivity analysis of an unstable steady-state flow solution around a circular bluff-bodies for different laminar Reynolds numbers, i.e. 60, 80, 100, 120, 140 and 160 computed using the free open-source FreeFEM++;
- Analyze and present of the impact of several control bluff-bodies of distinctive shapes and dimensions strategically put in the regions determined by the sensitivity analysis of a steady-state flow.

7.3. FUTURE WORK

This section presents present plausible continuations of the work presented in the current thesis, namely:

- Analyze the impact of several control bluff-bodies of distinctive shapes and dimensions strategically put in the regions determined by the sensitivity analysis of a mean flow solution;
- Extend the current work to turbulent flows, i.e. flow around bluff-bodies at Reynolds number higher than 2300. This implies the linearization and implementation of the *weak formulation* of the turbulence equations;
- Perform the linear global stability analysis and implicitly the sensitivity analysis of laminar three-dimensional flows to validate the linear global stability analysis equations expressed in cylindrical coordinate;
- Perform the linear global stability analysis and implicitly the sensitivity analysis of the flow inside the draft tube of the Francis-99 model turbine. Identify the onset region which lead to the apparition of the RVR;
- Test mathematical functions and physical methods such as water jet injections, aeration or insert physical objects to mitigate the RVR and therefore extending the operating range of the hydraulic turbine at the BEP.

REFERENCES

[1]T. I. Williams, *The History of Invention*. New York: Facts on File Publications, 1987.
[2]M. Gad-el-Hak, "Fluid mechanics from the beginning to the third millennium," *International Journal of Engineering Education*, vol. 14, no. 3, pp. 177–185, Jan. 1998.
[3]E. MacCurdy, *The Notebooks of Leonardo da Vinci*, vol. I and II. New York: Reynal & Hitchcock, 1938.
[4]Wikipedia Contributors, "Osborne Reynolds," *Wikipedia*, Sep. 17, 2019. https://en.wikipedia.org/wiki/Osborne_Reynolds
[5]P. K. Kundu and I. M. Cohen, *Fluid mechanics*, Second Edition. United States of America: Academic Press, 1990.
[6]Britannica, The Editors of Encyclopaedia, "Industrial Revolution | Definition, History, Dates, Summary, & Facts | Britannica Money," *www.britannica.com*, Jun. 08, 2023. https://www.britannica.com/money/topic/Industrial-Revolution
[7]European Environment Agency , "Global and European Temperatures," *www.eea.europa.eu*, Jun. 23, 2023. https://www.eea.europa.eu/ims/global-and-european-temperatures
[8]European Union, "EU measures against climate change | News | European Parliament," *www.europarl.europa.eu*, Jul. 08, 2018. https://www.europarl.europa.eu/news/en/headlines/society/20180703STO07129/eu-measures-against-climate-change
[9]European Council, "Infographic - How is EU electricity produced and sold?," *European Consilium*, May 10, 2023. https://www.consilium.europa.eu/en/infographics/how-is-eu-electricity-produced-and-sold/
[10]International Hydropower Association, "A brief history of hydropower," *www.hydropower.org*, 2022. https://www.hydropower.org/iha/discover-history-of-hydropower
[11]International Energy Agency, "Installed capacity in the European Union, 2000-2010, and projections up to 2040 in the Stated Policies Scenario – Charts – Data & Statistics," *IEA*, Oct. 27, 2020. https://www.iea.org/data-and-statistics/charts/installed-capacity-in-the-european-union-2000-2010-and-projections-up-to-2040-in-the-stated-policies-scenario
[12]H. Foroutan, "Simulation, Analysis, and Mitigation of Vortex Rope Formation in the

Draft Tube of Hydraulic Turbines," PhD Thesis, 2015.
[13]K Subramanya, *Hydraulic machines*. New Delhi: Mcgraw Hill Education (India) Private, 2015.
[14]J.-P. Franc, F. Avellan, and B. Belahadji, *La cavitation: M´ecanismes physiques et aspects industriels*. Grenoble: Presses Universitaires de Grenoble, 1995.
[15]C. Trivedi, M. Cervantes, and O. Dahlhaug, "Experimental and Numerical Studies of a High-Head Francis Turbine: A Review of the Francis-99 Test Case," *Energies*, vol. 9, no. 2, p. 74, Jan. 2016, doi: https://doi.org/10.3390/en9020074.
[16]Y. Jia, X. Wei, Q. Wang, J. Cui, and F. Li, "Experimental Study of the Effect of Splitter Blades on the Performance Characteristics of Francis Turbines," *Energies*, vol. 12, no. 9, p. 1676, May 2019, doi: https://doi.org/10.3390/en12091676.
[17]R. Goyal, "Flow Field in a High Head Francis Turbine Draft Tube During Transient Operations," PhD Thesis, Luleå University of Technology, 2017.
[18]S. Pasche, "Dynamics and Optimal Control of Self-Sustained Instabilities in Laminar and Turbulent Swirling Flows: Application to the Part Load Vortex Rope in Francis Turbines," PhD Thesis, ÉCOLE POLYTECHNIQUE FÉDÉRALE DE LAUSANNE, 2018.
[19]M. Nishi, S. Matsunaga, T. Kubota, and Y. Senoo, "Study on Swirl Flow and Surge in an Elbow Type Draft Tube," in *IAHR 11th Symposium: Operating problems of pump stations and power plant*, Amsterdam, 1980.
[20]A. Sébastien, "Forced and Self Oscillations of Hydraulic Systems Induced by Cavitation Vortex Rope of Francis Turbines," PhD Thesis, ÉCOLE POLYTECHNIQUE FÉDÉRALE DE LAUSANNE, 2011.
[21]D. H. Peckham and S. A. Atkinson, "Preliminary results of flow speed wind tunnel tests on a gothic wing of aspect ratio1.0," Aeronautical Research Council Current Paper No. 508, 1957.
[22]T. Sarpkaya, "On stationary and travelling vortex breakdowns," *Journal of Fluid Mechanics*, vol. 45, no. 3, pp. 545–559, Feb. 1971, doi: https://doi.org/10.1017/s0022112071000181.
[23]S. WANG and Z. RUSAK, "The dynamics of a swirling flow in a pipe and transition to axisymmetric vortex breakdown," *Journal of Fluid Mechanics*, vol. 340, pp. 177–223, Jun. 1997, doi: https://doi.org/10.1017/s0022112097005272.
[24]M. Kurosaka, M. Kikuchi, K. Hirano, T. Yuge, and H. Inoue, "Interchangeability of vortex-breakdown types," *Experiments in Fluids*, vol. 34, no. 1, pp. 77–86, Jan. 2003, doi: https://doi.org/10.1007/s00348-002-0535-3.
[25]F. Bunea, G. D. Ciocan, D. M. Bucur, G. Dunca, and A. Nedelcu, "Hydraulic Turbine

Performance Assessment with Implementation of an Innovative Aeration System," *Water*, vol. 13, no. 18, pp. 2459–2459, Sep. 2021, doi: https://doi.org/10.3390/w13182459.
[26]M. Nishi, X. M. Wang, K. Yoshida, T. Takahashi, and T. Tsukamoto, "An Experimental Study on Fins, Their Role in Control of the Draft Tube Surging," in *Hydraulic Machinery and Cavitation*, Netherlands: Dordrecht: Springer , 1996, pp. 905–914.
[27]R. Susan-Resiga, T. C. Vu, S. Muntean, G. D. Ciocan, and B. Nennemann, "Jet control of the draft tube vortex rope in Francis turbines at partial discharge," in *Proceedings of the 23th IAHR Symposium on HydraulicMachinery and Systems*, Yokohama, Japan, 2006.
[28]R. F. Susan-Resiga, S. Muntean, F. Avellan, and I. Anton, "Mathematical modelling of swirling flow in hydraulic turbines for the full operating range," *Applied Mathematical Modelling*, vol. 35, no. 10, pp. 4759–4773, Oct. 2011, doi: https://doi.org/10.1016/j.apm.2011.03.052.
[29]O. Reynolds, "An experimental investigation of the circumstances which determine whether the motion of water shall be direct or sinuous and of the law of resistance in parallel channels," in *Phil. Trans. Roy. Soc.*, 1883.
[30]Milton Van Dyke, *An Album of Fluid Motion*. Parabolic Press, Incorporated, 1988.
[31]Vassilios Theofilis, "Advances in global linear instability analysis of nonparallel and three-dimensional flows," *Progress in Aerospace Sciences*, vol. 39, no. 4, pp. 249–315, May 2003, doi: https://doi.org/10.1016/s0376-0421(02)00030-1.
[32]D. Barkley, "Linear analysis of the cylinder wake mean flow," *Europhysics Letters (EPL)*, vol. 75, no. 5, pp. 750–756, Sep. 2006, doi: https://doi.org/10.1209/epl/i2006-10168-7.
[33]S. Pasche, François Gallaire, and F. Avellan, "Predictive control of spiral vortex breakdown," *Journal of Fluid Mechanics*, vol. 842, pp. 58–86, May 2018, doi: https://doi.org/10.1017/jfm.2018.124.
[34]P. J. Strykowski and K. R. Sreenivasan, "On the formation and suppression of vortex 'shedding' at low Reynolds numbers," *Journal of Fluid Mechanics*, vol. 218, p. 71, Sep. 1990, doi: https://doi.org/10.1017/s0022112090000933.
[35]F. Giannetti and P. Luchini, "Structural sensitivity of the first instability of the cylinder wake," *Journal of Fluid Mechanics*, vol. 581, pp. 167–197, Jun. 2007, doi: https://doi.org/10.1017/s0022112007005654.
[36]O. Marquet, D. Sipp, and L. Jacquin, "Sensitivity analysis and passive control of cylinder flow," *Journal of Fluid Mechanics*, vol. 615, pp. 221–252, Nov. 2008, doi: https://doi.org/10.1017/s0022112008003662.
[37]Z. Seifi, M. Raisee, and M. K. Cervantes, "Global linear stability analysis of flow inside an axial swirl generator with a rotating vortex rope," *Journal of Hydraulic Research*, vol. 61,

no. 1, pp. 34–50, 2022, doi: https://doi.org/10.1080/00221686.2022.2106591.
[38]S. Pasche, F. Avellan, and François Gallaire, “Part Load Vortex Rope as a Global Unstable Mode,” *Journal of Fluids Engineering-transactions of The Asme*, vol. 139, no. 5, Mar. 2017, doi: https://doi.org/10.1115/1.4035640.
[39]J. S. Müller, F. Lückoff, T. L. Kaiser, and K. Oberleithner, “On the relevance of the runner crown for flow instabilities in a Francis turbine,” in *IOP Conference Series Earth and Environmental Science*, 2022.
[40]R. Betchov and W. O. Criminale, *Stability of Parallel Flow*. New York: Academic Press, 1967.
[41]R. Longobardi, “Fluid dynamic instabilities in complex flow systems,” PhD Thesis, 2019.
[42]K. Taira *et al.*, “Correction: Modal Analysis of Fluid Flows: An Overview,” *AIAA Journal*, vol. 58, no. 11, pp. AU9–AU9, Nov. 2020, doi: https://doi.org/10.2514/1.j056060.c1.
[43]P. Huerre and P. A. Monkewitz, “Absolute and convective instabilities in free shear layers,” *Journal of Fluid Mechanics*, vol. 159, no. -1, pp. 151–151, Oct. 1985, doi: https://doi.org/10.1017/s0022112085003147.
[44]François Charru, *Hydrodynamic Instabilities*. Cambridge University Press, 2011.
[45]P. Luchini and A. Bottaro, “Adjoint Equations in Stability Analysis,” *Annual Review of Fluid Mechanics*, vol. 46, no. 1, pp. 493–517, Jan. 2014, doi: https://doi.org/10.1146/annurev-fluid-010313-141253.
[46]J.-M. Chomaz, “GLOBAL INSTABILITIES IN SPATIALLY DEVELOPING FLOWS: Non-Normality and Nonlinearity,” *Annual Review of Fluid Mechanics*, vol. 37, no. 1, pp. 357–392, Jan. 2005, doi: https://doi.org/10.1146/annurev.fluid.37.061903.175810.
[47]P. J. Schmid, “Nonmodal Stability Theory,” *Annual Review of Fluid Mechanics*, vol. 39, no. 1, pp. 129–162, Jan. 2007, doi: https://doi.org/10.1146/annurev.fluid.38.050304.092139.
[48]E. L. Ince, *Edward L. Ince*. USA: Dover Publications, 1926.
[49]F. Hecht, “New development in freefem++,” *Journal of Numerical Mathematics*, vol. 20, no. 3–4, Jan. 2012, doi: https://doi.org/10.1515/jnum-2012-0013.
[50]“SALOME Geometry User’s Guide: Introduction to Geometry,” *docs.salome-platform.org*. https://docs.salome-platform.org/latest/gui/GEOM/index.html (accessed Sep. 15, 2023).
[51]C. Geuzaine and J.-F. Remacle, “Gmsh: A 3-D finite element mesh generator with built-in pre- and post-processing facilities,” *International Journal for Numerical Methods in Engineering*, vol. 79, no. 11, pp. 1309–1331, May 2009, doi: https://doi.org/10.1002/nme.2579.
[52]Houman Borouchaki, P.-L. George, and S. H. Lo, “OPTIMAL DELAUNAY POINT

INSERTION," *International Journal for Numerical Methods in Engineering*, vol. 39, no. 20, pp. 3407–3437, Oct. 1996, doi: https://doi.org/10.1002/(sici)1097-0207(19961030)39:20%3C3407::aid-nme5%3E3.0.co;2-c.
[53]F. Heicht, "BAMG: Bidimensional Anisotropic Mesh Generator," INRIA Report, 1998.
[54]D. Fabre *et al.*, "A Practical Review on Linear and Nonlinear Global Approaches to Flow Instabilities," *Applied Mechanics Reviews*, vol. 70, no. 6, Nov. 2018, doi: https://doi.org/10.1115/1.4042737.
[55]R. A. Dwyer, "A simple divide-and-conquer algorithm for computing Delaunay triangulations in O(n log log n) expected time," *Proceedings of the second annual symposium on computational geometry*, Jan. 1986, doi: https://doi.org/10.1145/10515.10545.
[56]P. L. George and P. Frey, "Mesh Generation: Application to Finite Elements," Hermes, Lyon, 2000.
[57]S. Rebay, "Efficient Unstructured Mesh Generation by Means of Delaunay Triangulation and Bowyer-Watson Algorithm," *Journal of Computational Physics*, vol. 106, no. 1, pp. 125–138, May 1993, doi: https://doi.org/10.1006/jcph.1993.1097.
[58]"Basic meshing algorithms — Mesh 9.11.0 documentation," *docs.salome-platform.org*. https://docs.salome-platform.org/latest/gui/SMESH/basic_meshing_algos.html#basic-meshing-algos-page (accessed Sep. 15, 2023).
[59]C. Canuto, *Spectral Methods in Fluid Dynamics*. 1988.
[60]E. Akervik, "Global stability and feedback control of boundary layer flows," PhD Thesis, Royal Institute of Technology, 2008.
[61]C. CFD, "The Differences Between Laminar vs. Turbulent Flow," *resources.system-analysis.cadence.com*. https://resources.system-analysis.cadence.com/blog/msa2022-the-differences-between-laminar-vs-turbulent-flow
[62]L. Mascotelli, "Direct Numerical Simulations of a turbulent pipe flow at high Reynolds numbers," PhD Thesis, POLITECNICO DI MILANO, 2016.
[63]B. Mulu, "An experimental and numerical investigation of a Kaplan turbine model," PhD Thesis, Luleå University of Technology, 2012.
[64]S. B. Pope, *Turbulent flows*. Cambridge ; New York: Cambridge University Press, 2000.
[65]J. Fröhlich and W. Rodi, "Introduction to large eddy simulation of turbulent flows," 2002.
[66]A. W. Leonard, "Energy Cascade in Large-Eddy Simulations of Turbulent Fluid Flows," *Advances in Geophysics*, vol. 18A, pp. 237–248, Jan. 1975, doi: https://doi.org/10.1016/s0065-2687(08)60464-1.
[67]M. Germano, U. Piomelli, P. Moin, and W. H. Cabot, "A dynamic subgrid-scale eddy viscosity model," *Physics of Fluids A: Fluid Dynamics*, vol. 3, no. 7, pp. 1760–1765, Jul.

1991, doi: https://doi.org/10.1063/1.857955.
[68]I. S. Grecu, “Contributions on the boundary layer flow numerical modelling in turbulent regime,” PhD Thesis, University Politehnica of Bucharest, 2023.
[69]M. Blakeslee, “Reynolds-Averaged Navier-Stokes (RANS) Simulations,” *2021.help.altair.com*. https://2021.help.altair.com/2021/hwsolvers/acusolve/topics/acusolve/training_manual/rans_simulations_r.htm
[70]B. Sun, “Revisiting the Reynolds-averaged Navier–Stokes equations,” *Open Physics*, vol. 19, no. 1, pp. 853–862, Jan. 2021, doi: https://doi.org/10.1515/phys-2021-0102.
[71]Ansys Inc., *ANSYS CFX-Solver Theory Guide*, Release 16.2, Help System, CFX Theory Manual.
[72]Code_Saturne, *Code_Saturne Theory Guide 7.0*. Paris: EDF R&D, 2021.
[73]D. C. Wilcox, *Turbulence modeling for CFD*. La Cañada, Calif. Dcw Industries, 2010.
[74]D. C. Wilcox, “Multiscale model for turbulent flows,” *AIAA Journal*, vol. 26, no. 11, pp. 1311–1320, Nov. 1988, doi: https://doi.org/10.2514/3.10042.
[75]N. A. Tonello, Y. Eude, B. de Laage de Meux, and M. Ferrand, “Frozen Rotor and Sliding Mesh Models Applied to the 3D Simulation of the Francis-99 Tokke Turbine with Code_Saturne,” *Journal of physics*, vol. 782, pp. 012009–012009, Jan. 2017, doi: https://doi.org/10.1088/1742-6596/782/1/012009.
[76]Code_Saturne, *Code_Saturne Theory Guide 7.0*. Paris: EDF R&D, 2021.
[77]N. Ottosen and H. Petterson, *Introduction to the Finite Element Method* , 1st ed. New York: Prentice Hall, 1992.
[78]D. Boffi, Franco Brezzi, and M. Fortin, *Mixed Finite Element Methods and Applications*. Springer Science & Business Media, 2013.
[79]T. Davis, “UMFPACK User Guide,” Dept. of Computer and Information Science and Engineering Univ. of Florida, Gainesville, FL, Jan. 2011.
[80]R. B. Lehoucq, D. C. Sorensen, and C. Yang, *ARPACK Users’ Guide*. SIAM, 1998.
[81]“Experimental study - NTNU,” *www.ntnu.edu*. https://www.ntnu.edu/nvks/f99-test-case1 (accessed Sep. 30, 2023).
[82]C. Trivedi, “Experimental and numerical investigations on steady state and transient characteristics of a high head Francis turbine,” PhD Thesis, Mechanical and Industrial Engineering Department, Indian Institute of Technology, Roorkee, India, 2014.
[83]R. Mitrut, Diana Maria Bucur, G. Dunca, and M. Cervantes, “Numerical Simulation of the Rotating Vortex Rope with Code_Saturne,” *2019 International Conference on ENERGY and ENVIRONMENT (CIEM)*, Oct. 2019, doi:

https://doi.org/10.1109/ciem46456.2019.8937583.
[84]R. Iovanel, “Numerical simulation of the flow in a Kaplan turbine,” PhD Thesis, University Politehnica of Bucharest, 2018.
[85]Gabriel Dan Ciocan, Monica Sanda Iliescu, T. Thu, Bernd Nennemann, and F. Avellan, “Experimental Study and Numerical Simulation of the FLINDT Draft Tube Rotating Vortex,” *Journal of Fluids Engineering-transactions of The Asme*, vol. 129, no. 2, pp. 146–158, Feb. 2007, doi: https://doi.org/10.1115/1.2409332.
[86]R Mitruţ, Diana Maria Bucur, G. Dunca, and M. J. Cervantes, “Global linear stability analysis of the flow inside a conical draft tube,” *IOP Conference Series Earth and Environmental Science*, vol. 1079, no. 1, pp. 012049–012049, Sep. 2022, doi: https://doi.org/10.1088/1755-1315/1079/1/012049.
[87]A. Minakov, D. Platonov, A. Sentyabov, and A. Gavrilov, “Francis-99 turbine numerical flow simulation of steady state operation using RANS and RANS/LES turbulence model,” *Journal of Physics: Conference Series*, vol. 782, p. 012005, Jan. 2017, doi: https://doi.org/10.1088/1742-6596/782/1/012005.
[88]J. Ignacio Jimenez Gonzalez, “Study of the stability of jets and wakes. Application to the wake past slender bodies with blunt trailing edge,” PhD Thesis, UNIVERSIDAD DE JAEN, 2013.
[89]B. R. Noack and Helmut Eckelmann, “A global stability analysis of the steady and periodic cylinder wake,” *Journal of Fluid Mechanics*, vol. 270, pp. 297–330, Jul. 1994, doi: https://doi.org/10.1017/s0022112094004283.
[90]M. Provansal, C. Mathis, and L. Boyer, “Bénard-von Kármán instability: transient and forced regimes,” *Journal of Fluid Mechanics*, vol. 182, no. -1, pp. 1–1, Sep. 1987, doi: https://doi.org/10.1017/s0022112087002222.
[91]R. Mitrut, Diana Maria Bucur, G. Dunca, and M. Cervantes, “Linear Global Stability Analysis of a Laminar Flow Around a Circular Body,” *12th International Symposium on Advanced Topics in Electrical Engineering (ATEE)*, Mar. 2021, doi: https://doi.org/10.1109/atee52255.2021.9425105.
[92]“MathWorks - Makers of MATLAB and Simulink,” *Mathworks.com*, 2019. https://www.mathworks.com
[93]“ParaView,” *Paraview.org*, 2018. https://www.paraview.org/
[94]O. Marquet and M. Carini, “Extended mean flow analysis of the circular cylinder flow,” *arXiv: Fluid Dynamics*, 2020, doi: https://doi.org/10.48550/arXiv.2008.10002.
[95]C. H. K. Williamson, “Vortex Dynamics in the Cylinder Wake,” *Annual Review of Fluid Mechanics*, vol. 28, no. 1, pp. 477–539, Jan. 1996, doi:

https://doi.org/10.1146/annurev.fl.28.010196.002401.
[96]Ján Dušek, Patrice Le Gal, and Philippe Fraunié, “A numerical and theoretical study of the first Hopf bifurcation in a cylinder wake,” *Journal of Fluid Mechanics*, vol. 264, pp. 59–80, Apr. 1994, doi: https://doi.org/10.1017/s0022112094000583.
[97]Willem, “Outline of a theory of turbulent shear flow,” *Journal of Fluid Mechanics*, vol. 1, no. 5, pp. 521–539, Nov. 1956, doi: https://doi.org/10.1017/s0022112056000342.
[98]J. T. Stuart, “Nonlinear Stability Theory,” *Annual Review of Fluid Mechanics*, vol. 3, no. 1, pp. 347–370, Jan. 1971, doi: https://doi.org/10.1146/annurev.fl.03.010171.002023.
[99]D. Sipp, O. Marquet, P. Meliga, and A. Barbagallo, “Dynamics and Control of Global Instabilities in Open-Flows: A Linearized Approach,” *Applied Mechanics Reviews*, vol. 63, no. 3, Apr. 2010, doi: https://doi.org/10.1115/1.4001478.
[100]R. Mitrut, Diana Maria Bucur, G. Dunca, and M. Cervantes, “Numerical Simulation of Vortex Breakdown with Code Saturne,” *2021 10th International Conference on ENERGY and ENVIRONMENT (CIEM)*, Oct. 2021, doi: https://doi.org/10.1109/ciem52821.2021.9614834.